Journal of Volcanology and Geothermal Research 443 (2023) 107919

Contents lists available at ScienceDirect

Journal of Volcanology and Geothermal Research

journal homepage: www.journals.elsevier.com/journal-of-volcanology-and-geothermal-research

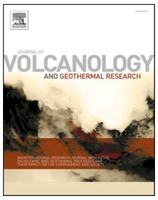

Dynamics of the Young Merapi (<2.2 ka – 1,788 CE) pumice fall deposits: Insights from textural and geochemical studies

Indranova Suhendro [a,b,*], Gabriela Nogo Retnaningtyas Bunga Naen [c,d], Andriansyah Gurusinga [e], Sistien Adhaena Sari [f], Mradipta Lintang Alifcanta Moktikanana [e], Rachmi Mustika Pertiwi Putri Gunawan [g], Jesslyn Jane [h], Muhammad Fatih Qodri [i], Faraz Sya'bana [j], Sherinna Mega Cahyani [h], Dini Nuari Ardian [k]

[a] *Department of Environmental Geography, Faculty of Geography, Universitas Gadjah Mada, Sekip Utara Jl. Kaliurang, Bulaksumur, Yogyakarta 55281, Indonesia*
[b] *Center for Disaster Studies, Universitas Gadjah Mada, Jl. Mahoni C-16 Bulaksumur, 55281 Yogyakarta, Indonesia*
[c] *Department of Earth and Planetary Sciences, Graduate School of Science, Kyushu University, Nishiku, 744, Motooka, Fukuoka 819-0395, Japan*
[d] *Research Center for Geological Disaster, National Research and Innovation Agency of the Republic of Indonesia (BRIN), Bandung 40135, Indonesia*
[e] *Department of Earth Resource Science, Akita University, 1-1, Tegata Gakuenmachi, Akita 010-8502, Japan*
[f] *School of Environment, University of Auckland, New Zealand*
[g] *Balai Besar Pengujian Minyak dan Gas Bumi "LEMIGAS", Ministry of Energy and Mineral Resources, Indonesia*
[h] *Geological Engineering Department, Faculty of Engineering, Universitas Gadjah Mada, Jl. Grafika No.2, 55281, Indonesia*
[i] *Geological Engineering Department, Institut Teknologi Nasional Yogyakarta, Indonesia*
[j] *PT Ricobana Abadi, Sambarata Mine Operation, PT Berau Coal, Berau, East Kalimantan, Indonesia*
[k] *Dongeng geologi, Jakarta, Indonesia*

ARTICLE INFO

Keywords:
Merapi volcano
Young Merapi
Pumice fall deposits
Vesicle number density
Microlite number density
Magma decompression rate

ABSTRACT

We studied nine pumice fall deposits of the Young Merapi stage (<2.2 ka – 1,788 CE) observed in the western and southern flanks of Merapi volcano. All deposits include a wide variation of lithics (10–42% C_{lithic}), with thicker deposits (i.e., more voluminous eruption) being more lithic-rich and vice versa. Two different magma types (hereafter referred to as type I and type II) were identified based on petrography, bulk-rock, glass, and feldspar microlite compositions. Type I magma has abundant amphibole and pyroxene, is rich in calcium (>9 wt% CaO_{bulk}), poor in both silica (50.8–53.7 wt% SiO_{2bulk} and 62.3–66.6 wt% SiO_{2glass}) and strontium (<580 ppm, bulk-rock), and has more calcic feldspar microlites ($An_{38–79}$). Type II magma also contains abundant amphibole, but has less pyroxene and is poorer in calcium (<9 wt% CaO_{bulk}), higher in both silica (53.2–54.5 wt% SiO_{2bulk} and 63.3–70.8 wt% SiO_{2glass}) and strontium (>580 ppm), with less calcic feldspar microlites ($An_{31–77}$). These two magma types alternately fed the explosive eruptions during the Young Merapi stage; however, their juvenile products are distinctive in terms of *syn*-eruptive microtextures (i.e., matrix-vesicles and microlites). Pumices from type II magma have a higher matrix-vesicle number density (MVND) and microlite number density (MND) values than those of pumices from type I magma (1.0–6.5 × 10^{15} and 1.8–7.4 × 10^{15} m^{-3}, and 0.6–2.3 × 10^{15} and 0.7–1.8 × 10^{15} m^{-3}, respectively). A positive correlation between MVND with SiO_2 and MND suggests that a colder (i.e., less calcic feldspar microlites indicate lower temperature and vice versa) and more evolved (higher SiO_2) magma facilitates more extensive matrix-bubble nucleation and deeper microlite crystallization than hotter magmas, allowing type II magma to erupt more explosively than type I magma.

1. Introduction

Merapi volcano is one of the basaltic-basaltic andesite stratovolcanoes in Indonesia (Newhall et al., 2000; Gertisser et al., 2012; Innocenti et al., 2013; Gertisser et al., 2023) (Fig. 1), formed by the northward subduction of the Indo-Australian plate towards the Eurasian plate, and considered as the youngest member of the Central Java Quaternary volcanic belt (Phuong et al., 2012). Merapi volcano is also

---

* Corresponding author at: Department of Environmental Geography, Faculty of Geography, Universitas Gadjah Mada, Sekip Utara Jl. Kaliurang, Bulaksumur, Yogyakarta 55281, Indonesia.
E-mail address: indranova.suhendro@ugm.ac.id (I. Suhendro).

https://doi.org/10.1016/j.jvolgeores.2023.107919
Received 19 December 2022; Received in revised form 27 July 2023; Accepted 25 September 2023

known as one of the most active and dangerous volcanoes in the world (Lavigne et al., 2000); not only because it frequently produces block and ash pyroclastic density currents (PDCs) via dome collapses (Andreastuti et al., 2000; Kelfoun and Gueugneau, 2022) and aftermath lahars (Lavigne et al., 2000; de Bélizal et al., 2013; Hadmoko et al., 2018), but also widely dispersed tephra falls from buoyant eruption plumes with volcano explosivity indices (VEIs) up to 4 (Andreastuti et al., 2000; Gertisser et al., 2012; Solikhin et al., 2015). However, our understanding of the dynamics of pumice fall-associated explosive eruptions at Merapi remains limited, as most of the previous studies focused on the aspect of general-stratigraphic framework, storage conditions, lava domes, PDCs, and lahars (Andreastuti et al., 2000, Newhall et al., 2000, Gertisser et al., 2012; van der Zwan et al., 2013, Costa et al., 2013; Darmawan et al., 2022; Shimomura et al., 2019, Kelfoun and Gueugneau, 2022; Lavigne et al., 2000, de Bélizal et al., 2013, Hadmoko et al., 2018). Moreover, understanding the explosive behavior of basalt-basaltic andesite magmas represents an important challenge since (1) many basalt-basaltic andesite volcanoes are located adjacent to human settlements (e.g., Arenal in Costa Rica, Izu-Oshima in Japan, Merapi and Kelud in Indonesia, Calbuco in Chile, Mayon in the Philippines; Streck and Wacaster, 2006, Ikehata et al., 2010, Gertisser et al., 2012, Maeno et al., 2019, Namur et al., 2020, Ruth and Costa, 2021), and (2) they are capable of producing VEI 4–5 eruptions, such as Merapi and Kelud in Indonesia, Izu-Oshima in Japan, and Llama in Chile (Gertisser et al., 2012; Maeno et al., 2019; Ikehata et al., 2010; Marshall et al., 2022). To shed light on this issue, we studied nine pumice fall deposits from the Young Merapi stage (<2.2 ka – 1,788 CE). Three of them were identified as Trayem, Jurangjero 1, and Jurangjero 2 tephras due to the significant similarity in deposit characteristics reported by Gertisser et al. (2012).

Starting from the stratigraphical descriptions of tephra deposits

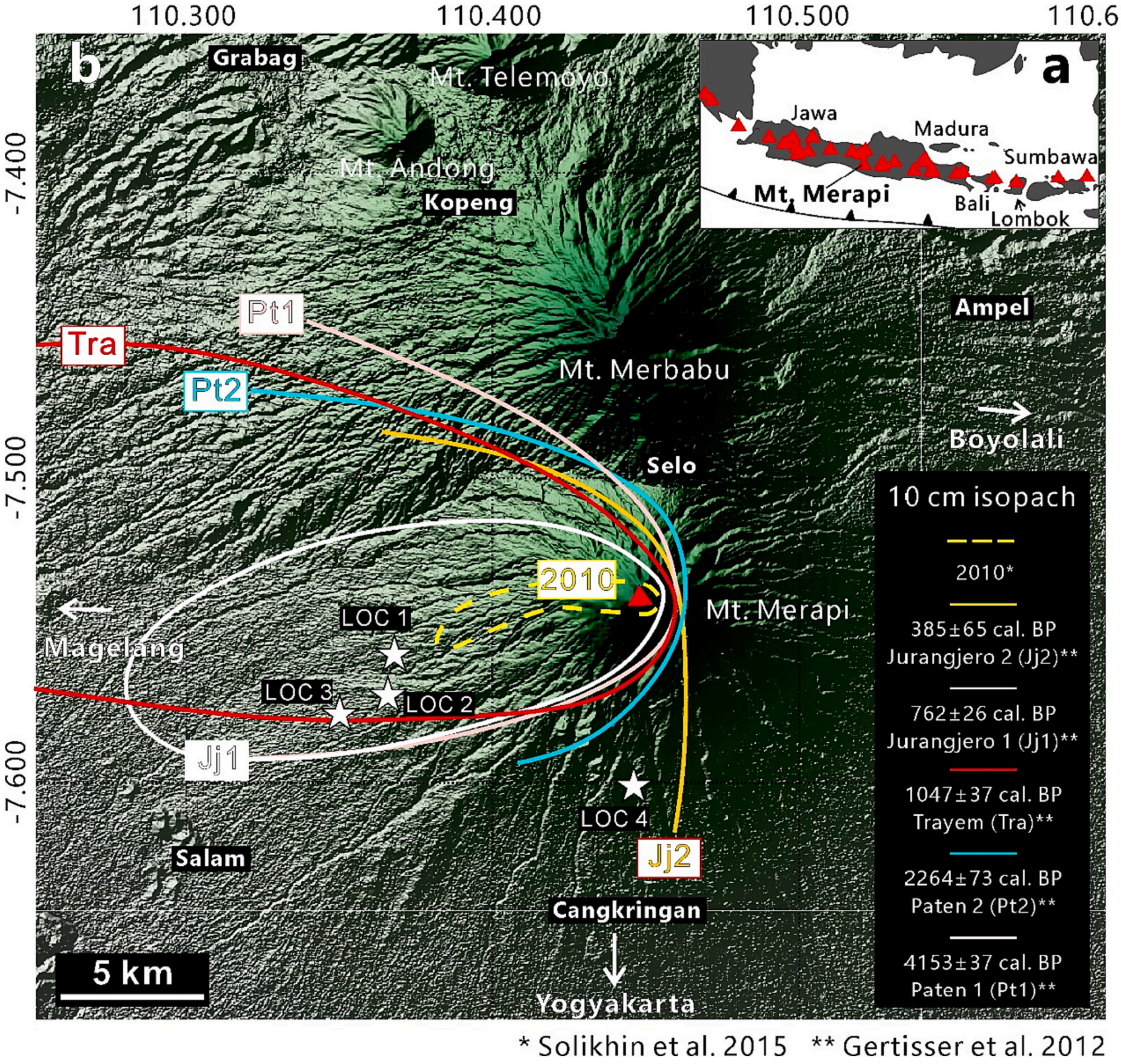

Fig. 1. (a) A sketch map showing the location of Merapi volcano in Central Java, Java Island. Red triangles are active volcanoes, while grey area represent islands. Black solid line with triangles is the subduction zone between Indo-Australia and Eurasia. (b) 10-cm isopach of some VEI 3–4 eruptions of Merapi volcano (Paten I, Paten II, Trayem, Jurangjero I, Jurangjero II, and 2010 CE) obtained from Gertisser et al., 2012 and Solikhin et al., 2015. Our sampling locations were focused on the western flanks because, all of those fall deposits were distributed to west side (towards Magelang City). We visited the southern flank with aim to sample an unnamed Young Merapi pumice fall deposit (~20–30 cm-thick) as reported in Gertisser et al. (2011; see their Fig. 7c). Digital elevation model image was obtained from Badan Informasi Geospasial (BIG) Indonesia 2022. (For interpretation of the references to colour in this figure legend, the reader is referred to the web version of this article.)

observed on the western and southern sides of the Merapi volcano, we report the quantitative results of componentry, petrography (i.e., phenocryst fraction, mineral assemblages), vesicles and microlites (i.e., volume fraction and number density), as well as the chemical compositions of bulk-rock, glass, and feldspar phenocrysts and. Petrographic and chemical analyses were used to evaluate the pre-eruptive magma storage conditions. Textural studies of vesicles and microlites were used to support the interpretation of magma storage conditions, as well as to investigate the *syn*-eruptive conduit processes.

2. Overview of the Merapi volcano

2.1. Brief history

The activity of Merapi volcano is divided into four main episodes: Ancient, Middle, Young, and Modern (Berthommier, 1990; Camus et al., 2000; Gertisser et al., 2012; Gertisser et al., 2023). The Ancient period is represented by Turgo, Plawangan, and Medjing Hills, which are interpreted as the lava flows of the Proto-Merapi volcanic edifice, erupted between 138 and 135 ± 3 ka (Gertisser et al., 2012, 2023) or ± 40–14 ka (Berthommier, 1990; Camus et al., 2000). Since then, activity during the Middle period took place at the Old Merapi volcanic edifice (Somma-Merapi; Gertisser et al., 2012, 2023), producing subsequent lava flows (the identified ages are 109 ± 60 ka, 30.3 ± 1 ka, 29.4 ± 1 ka, 24.2 ± 0.8 ka, 10.7 ± 0.8 ka, 8.6 ± 1.4 ka, and 4.8 ± 1.5 ka; Gertisser et al., 2012, 2023) with some series of pyroclastic fall and pyroclastic density current (PDC) deposits emplaced during the period of 11,792 ± 90 to 2264 ± 73 cal. BP (Gertisser et al., 2012, 2023) or ± 14.0–2.2 ka (Berthommier, 1990, Camus et al., 2000). The eruptive activity during the Young and Modern period (<2.2 ka–1,786 CE and younger than 1,786 CE, respectively; Gertisser et al., 2012, Berthommier, 1990, Camus et al., 2000) took place from the Young Merapi (post-Somma-Merapi) volcanic edifice, producing abundant pyroclastic falls, PDCs, lava flows, and/or lava domes with VEI ranging from 1 to 4 (Gertisser et al., 2012; Surono et al., 2012; Cronin et al., 2013; Gertisser et al., 2023).

Detailed studies on stratigraphy (e.g., Andreastuti et al., 2000; Newhall et al., 2000; Gertisser et al., 2012, 2023) have revealed that Merapi volcano experienced multiple moderate-explosive eruptions (VEI 3–4) with sub-Plinian to Plinian intensity, as indicated by the presence of abundant pumice and/or scoria fall deposits and PDC layers. Some of these VEI 3–4 eruptions occurred at <4153 ± 37 cal. BP (Paten I), 2264 ± 73 cal. BP (Paten II), 1047 ± 37 cal. BP (Trayem), 762 ± 26 cal. BP (Jurangjero I), 385 ± 65 cal. BP (Jurangjero II), 1872 CE, and 2010 CE (Andreastuti et al., 2000, Newhall et al., 2000, Gertisser et al., 2012, Surono et al., 2012, Cronin et al., 2013, Solikhin et al., 2015, Gertisser et al., 2023) (Fig. 1). However, the 1872 and 2010 CE eruptions have been associated with PDCs instead of fall deposits (Newhall et al., 2000; Surono et al., 2012; Cronin et al., 2013; Solikhin et al., 2015). Many studies suggest that a large, catastrophic eruption also occurred in 1006 CE, with an intensity similar to that of the 1980 CE eruption of St. Helens, and is thus responsible for generating the sector collapse event of Somma-Merapi (e.g., Van Bemmelen, 1949; Berthommier, 1990; Camus et al., 2000). Gendol Hills in the southwestern side of Merapi (ca. ±18 km from the summit) is therefore suggested to be the 1006 CE hummocks (i.e., the product of the debris avalanche). However, Newhall et al. (2000) provide an alternative interpretation: Gendol Hills represents the remnant of an older volcanic edifice since (1) a new K—Ar dating from one of the hills suggests a significantly older age (3.44 ± 0.09 Ma); (2) it lacks the characteristics of debris avalanche deposits such as jigsaw brecciation and block facies/matrix facies relationships; and (3) the lithology of hornblende-pyroxene andesite is similar to those found in Menoreh Mountains (an ancient volcanic edifice located ±7 km to the west of Gendol Hills).

2.2. The developed magma plumbing system

Through petrological and geophysical investigations, previous studies have shown that the magma plumbing system beneath Merapi volcano is quite complex, containing numerous vertically-distributed magmatic reservoirs, ranging from 700 MPa to 100 MPa (e.g., Costa et al., 2013; Chadwick et al., 2013; van der Zwan et al., 2013; Widiyantoro et al., 2018). Specifically, the plumbing system has been divided into three levels (deep, intermediate, and shallow), where each reservoir is located at pressures >600, 500–200, and < 200 MPa, respectively (Costa et al., 2013; Widiyantoro et al., 2018). In such a complex plumbing system, two magmatic affinities of basalt-basaltic andesite compositions are observed: the medium-K and high-K (MK and HK, respectively) (Gertisser and Keller, 2003; Gertisser et al., 2012, 2023). The Ancient and Middle periods includes both types (MK and HK), while the Young and Modern periods are exclusive to HK magma (Gertisser et al., 2023, see their Fig. 6.18). Moreover, the products of Merapi are typically rich in amphibole, suggesting a hydrous magmatic system with at least 4–6 wt% of water (Costa et al., 2013; Innocenti et al., 2013).

3. Methods

3.1. Fieldwork activities and sampling strategies

Fieldwork was conducted for sampling purposes, as well as to record the essential elements in the observed deposits, including deposit structure (i.e., massive and/or graded), clast types and sizes, and stratigraphy. We established 4 observation locations on the western (LOC 1, 2, and 3) and southern (LOC 4) flanks of Merapi volcano (Fig. 1). Most of the observation locations were established on the western flank because the isopach maps provided by previous studies (i.e., Gertisser et al., 2012; Solikhin et al., 2015) (Fig. 1) suggested that most pumice fall deposits were emplaced to the west (Fig. 1). We also visited the southern flank because we aimed to sample an unnamed Young Merapi pumice fall deposit (~20–30 cm-thick) as reported in Gertisser et al. (2011); (see their Fig. 7c).

Each pumice fall deposit was sampled at a locality about 8–9 km from the present vent, where the outcrop displays fresh conditions (Figs. 1 and 2). The studied samples were collected from the main fallout layer and, if present, from sub-layers (shown as blue star symbol in Fig. 3) for further laboratory analyses, including grain size distribution (GSD), componentry, chemical (bulk-rock, glass, and mineral chemistry) and textural analyses.

3.2. Grain size distribution (GSD) and componentry

A total of 11 samples (including the main fallout layer and, sub-layers) were used for GSD and componentry analyses, namely F1—P, F2—P, F3—P, F4—P, Tra-LP, Tra-UP, F5—P, Jj1-P, Jj2-LP, Jj2-UP, and F6—P (Fig. 4). Samples were dried in an oven at 120 °C for 24 h and subsequently sieved using -6Φ to 4Φ (>32 to <1/16 mm) mesh sizes under 1-phi intervals to obtain the distribution of grain size. Componentry analysis was obtained by observing the size fraction between -6Φ and -2Φ (>32 to 4 mm) under the naked eye (for particles larger than 16 mm) and stereomicroscope (for 4–16 mm particles). We classified the particles in pumice, scoria, lithics and free crystals based on their qualitative characteristics, such as colour, shape, brightness, transparency, and/or vesicles (Fig. 4a).

3.3. Petrography

We studied (at most) three thin sections of pumice clasts (depending on the texture variabilities, i.e., vesicles) from each eruption (F1—P, F2—P, F3—P, F4—P, Tra, F5—P, Jj1-P, Jj2-P, and F6—P) to qualitatively observe the mineral textures (e.g., zoning, sieving) and their variations

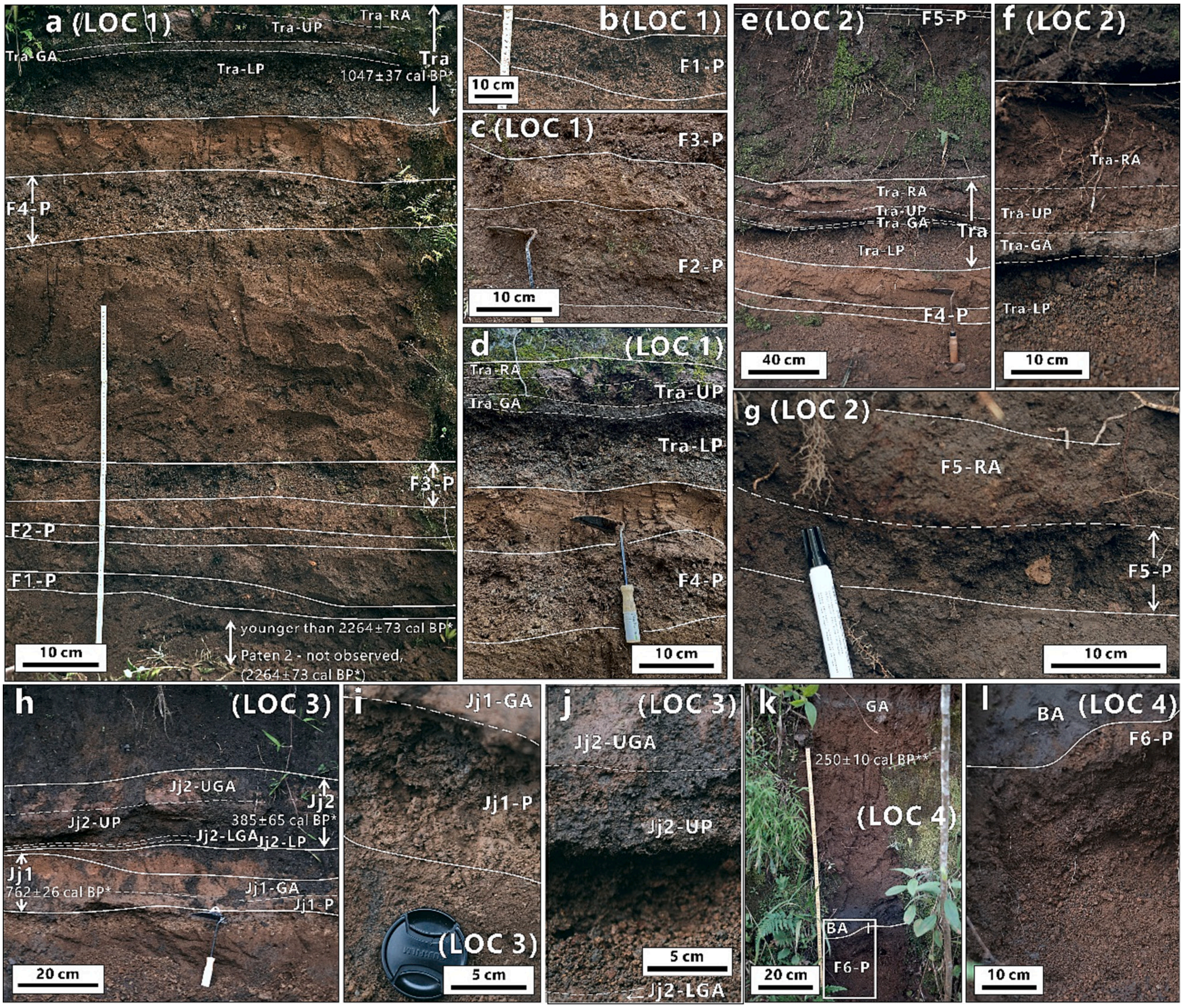

Fig. 2. (a) Outcrop image of LOC 1, consisting of five pumice fall layers (F1—P, F2—P, F3—P, F4—P, and Trayem (Tra)). The absence of Paten I and II deposits (4153 ± 37 and 2264 ± 37 cal. BP, respectively; Gertisser et al., 2012), coupled with the presence of Trayem deposit (1047 ± 37 cal. BP; Gertisser et al., 2012) in the uppermost part strongly suggest that these deposits correspond to the Young Merapi stage. Tra-LP, Tra-GA, Tra-UP, and Tra-RA correspond to Trayem lower pumice, Trayem grey ash, Trayem upper pumice and Trayem reddish ash, respectively. Detailed image of F1—P (b), F2—P, F3—P (c), F4—P and Trayem deposits (d). (e, f) Outcrop image of LOC 2, showing the occurrence of F5—P above the Trayem deposit. (g) Detailed image of F5—P and F5-RA layer (pumice and reddish ash, respectively), showing a relatively darker colour compared to the other observed pumice fall layers. (h) Outcrop image of Jurangerjo I and Jurangjero II pumice fall deposits (762 ± 26 and 385 ± 65 cal. BP, respectively; Gertisser et al., 2012) at LOC 3. Detailed image of Jurangjero I pumice (Jj1-P) and grey ash (Jj1-GA) (i), and Jurangjero II lower grey ash (Jj2-LGA), upper pumice (Jj2-UP), and upper grey ash (Jj2-UGA) (j). (k) Outcrop image of LOC 4, showing the occurrence of F6—P layer, which is positioned below black ash (BA) and a 250 ± 10 cal. BP charcoal-rich pyroclastic density current (PDC) deposit (Newhall et al., 2000).

(Fig. 5). A mosaic of BSE images (acquired by means of a scanning electron microscope; Fig. 6) for each thin section was used to quantify pheno-crystallinity (porphyricity index) and mineral assemblages. We digitized all phenocryst phases (each mineral phase being represented by a different colour) using a graphic design software (e.g., Corel Draw, Adobe Illustrator) and processed the resultant images using the software Image-J to obtain the number and size of the phenocrysts. The vesicle-free phenocryst content ($\mathring{\varphi}_{PC}$) was obtained using the following equation (e.g., Klug and Cashman, 1994; Gurioli et al., 2005; Suhendro et al., 2022):

$$\mathring{\varphi}_{PC} = \frac{\varphi_{PC}}{1-\varphi_{BV}} \tag{1}$$

where φ_{PC} is the vesicle-included pheno-crystallinity obtained by dividing the total area of phenocrysts with total grain area, and φ_{BV} is the bulk-vesicularity obtained by dividing the total area of vesicles with total grain area.

3.4. Bulk-rock, glass, and feldspar phenocryst and microlite compositions

Bulk-rock composition was obtained using RIGAKU ZSX Primus II at the Department of Earth Resource Science, Akita University. 18 juvenile samples from 9 pumice fall layers (F1—P, F2—P, F3—P, F4—P, Tra, F5—P, Jj1-P, Jj2-P, and F6—P) were selected for this analysis (each layer is represented by 1–3 measurements, depending on the existence of sub-layer and sample availability) (Fig. 7). The juvenile clasts (grouped for componentry) were analyzed using glass beads method. First, samples were powdered using tungsten mill, annealed at 900 °C, and diluted with 1:5 ratio of rock samples and mixture of lithium borate ($Li_2B_4O_7$) and lithium metaborate ($LiBO_2$). Subsequently, we fused the powder at 1150 °C to make glass beads. Finally, glass beads were analyzed to obtain the major and trace element compositions using matrix-corrected

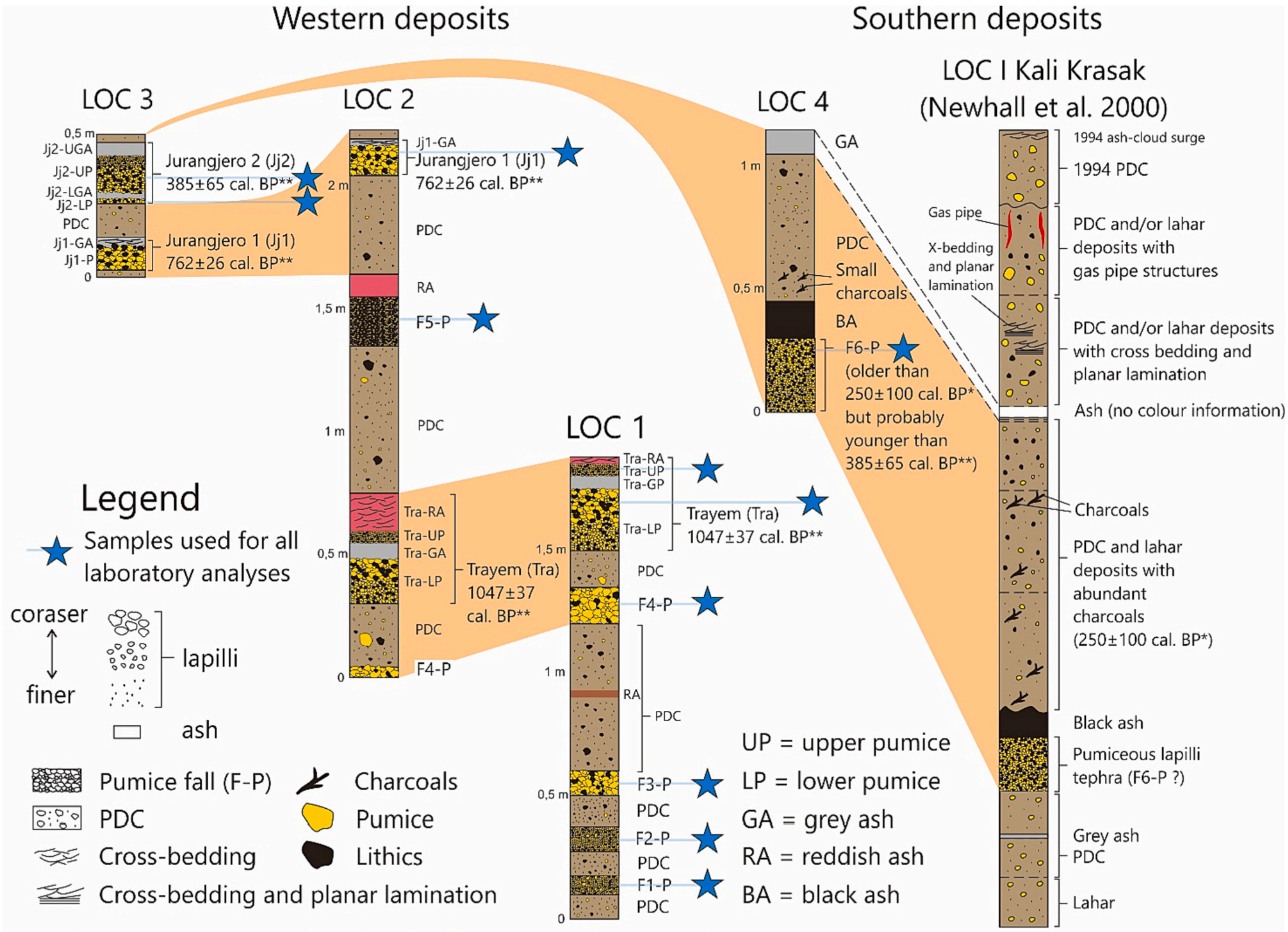

*) ^{14}C-dating by Newhall et al. 2000 **) ^{14}C-dating by Gertisser et al. 2012

Fig. 3. Stratigraphy correlation of four different locations. Note that LOC 4 in the south flank include no equivalent layer to those of west flank deposits. However, according to Newhall et al. (2000), the black ash (BA; older than 250 ± 10 cal. BP) layer is only observed at LOC I – Kali Krasak, thus become our key layer to identify the relative position of F6—P layer with the western flank deposits.

calibration curves from standard samples of igneous rock series from the Geological Survey of Japan (GSJ).

The composition of groundmass glasses and feldspar phenocrysts and microlites was obtained using JEOL JXA 8530-F Field Emission Electron Microprobe (FE-EPMA) at the Faculty of Science, Kyushu University, using a focused beam with 1 μm diameter size and 15 kV accelerating voltage (Figs. 7 and 8). For groundmass glasses, each clast is represented by five to ten measurement locations, avoiding cracks and microlites (note that the number of measured glasses compositions depends on the microlite abundance). For phenocrysts, each clast is represented by ten crystals, and each core and rim composition were represented by the average anorthite value (obtained from three measurement locations, avoiding cracks and inclusions). For microlites, we only report the core compositions (one measurement point for each crystal) because the rim size was typically smaller than the beam diameter.

3.5. *Quantifying vesicles*

Many studies have suggested that magmas experienced two stages of vesiculation, before and during the eruption (named pheno- and matrix-bubbles, respectively) (e.g., Toramaru, 2014; Edmonds and Woods, 2018; Suhendro et al., 2022). To define the boundary between pheno- and matrix-vesicles, we performed 2D-vesicle size distribution (VSD) measurements for each thin section (which were also used for petrography analysis and quantification of microlites; see also Sections 3.3 and 3.6.) under three image scales: mosaic (varying from 84 to 212 mm^2), 200× magnification (0.48 mm^2), and 500× magnification (0.09 mm^2) (Fig. 6). Both vesicle populations (i.e., pheno- and matrix-vesicles) can experience bubble coalescence process during eruption. Thus, de-coalescing the vesicle morphology via manual digitation (using a graphic design software) is essential to capture the most actual volume fraction and number densities of pheno- and matrix-vesicles (Klug and Cashman, 1994, 1996). Subsequently, the digitized vesicle images were processed using image-J software to obtain the number and area of vesicle. Finally, the number density of pheno- and matrix-vesicles (PVND and MVND, respectively) were obtained from eqs. 2 and 3, assuming homogeneous-spherical vesicles shape (e.g., Klug and Cashman, 1994; Gurioli et al., 2005, and Suhendro et al., 2022):

$$PVND\ (N_V) = (N_{APV}/D_{PV})\big/\left(1-\varphi^{*}_{BV}\right) \tag{2}$$

$$MVND\ (N_V) = (N_{AMV}/D_{MV})/(1-\varphi_{MV}) \tag{3}$$

where N_{APV} is number density per unit area of pheno-vesicle, D_{PV} is the average pheno-vesicle size, N_{AMV} is number density per unit area of matrix-vesicle, D_{MV} is the average matrix-vesicle size, φ^{*}_{BV} is phenocryst-free bulk-vesicularity (i.e., summation of pheno-vesicle and matrix-vesicle fractions in a whole grain without phenocrysts), and φ_{MV} is matrix-vesicularity (i.e., fraction of matrix-vesicle in the entire clast groundmass).

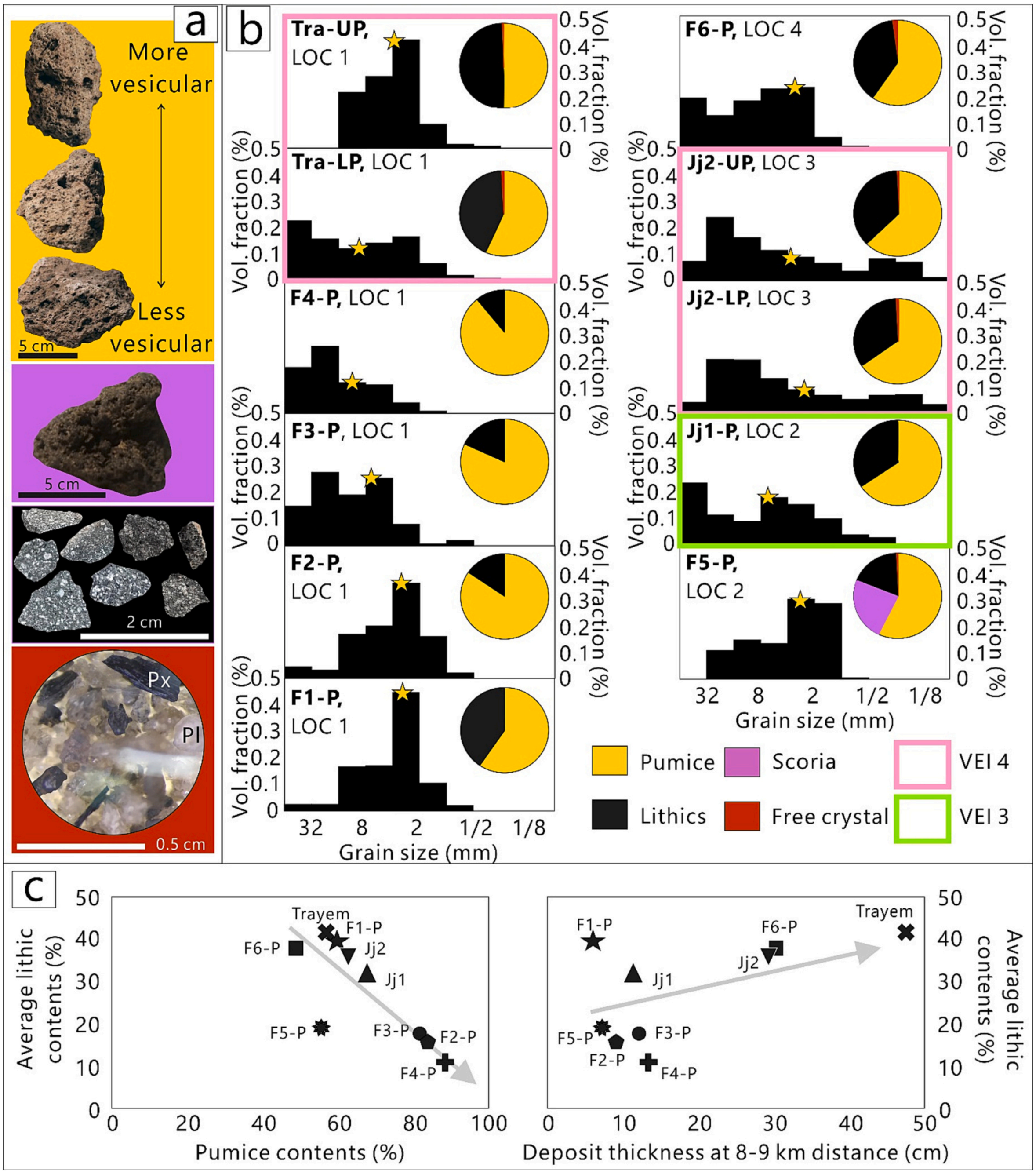

Fig. 4. (a, b) Component variations, grain size distribution (GSD) and componentry results of the Young Merapi pumice fall deposits. Yellow star in GSD chart represents median size. Yellow, purple, black, and red in pie chart denotes pumice, scoria, lithics, and free crystals, respectively. The volcano explosivity index (VEI) refers to Gertisser et al. (2012), where pink and green squares represent VEI 3 and 4 eruptions, respectively. (c) Bivariate plots between average lithic contents with pumice contents (left) and deposit thickness at 8–9- km distance from the vent (right). (For interpretation of the references to colour in this figure legend, the reader is referred to the web version of this article.)

3.6. *Quantifying crystals*

Previous studies have suggested that crystals in volcanic rocks can be defined to three phases: microlite, microphenocryst, and phenocryst (e.g., Hammer et al., 1999; Polacci et al., 2001; Gurioli et al., 2005; Salisbury et al., 2008; Humphreys et al., 2009; Shea et al., 2009; Shea et al., 2012). Thus, it is important to define their specific size quantitatively via image processing. Similar to vesicles, we determine the boundary between each crystal phase by performing size distribution analysis (for each thin section; Figs. 9 and 10) under three image magnifications, i.e., mosaic, 200×, and 500× (see previous section). However, because distinguishing plagioclase and glass in the BSE images was very difficult due to the lack of colour contrast (Fig. 6), we chose pyroxene as it is considered as one of the most abundant mineral phases (both as large and small crystal sizes). Pyroxenes from each magnification were manually digitized using a graphic-design software and processed by Image-J to obtain the number and size. The results from ImageJ were exported to *CSDslice* program to determine the crystal aspect ratio, following the methods of Morgan and Jerram (2006). The average aspect ratio of pyroxene crystals was found to be 1.0:1.5:2.5, while the roundness factor was set at 0.0. Afterwards, the crystal size distribution (CSD) of pyroxene was determined using *CSDcorrections* software,

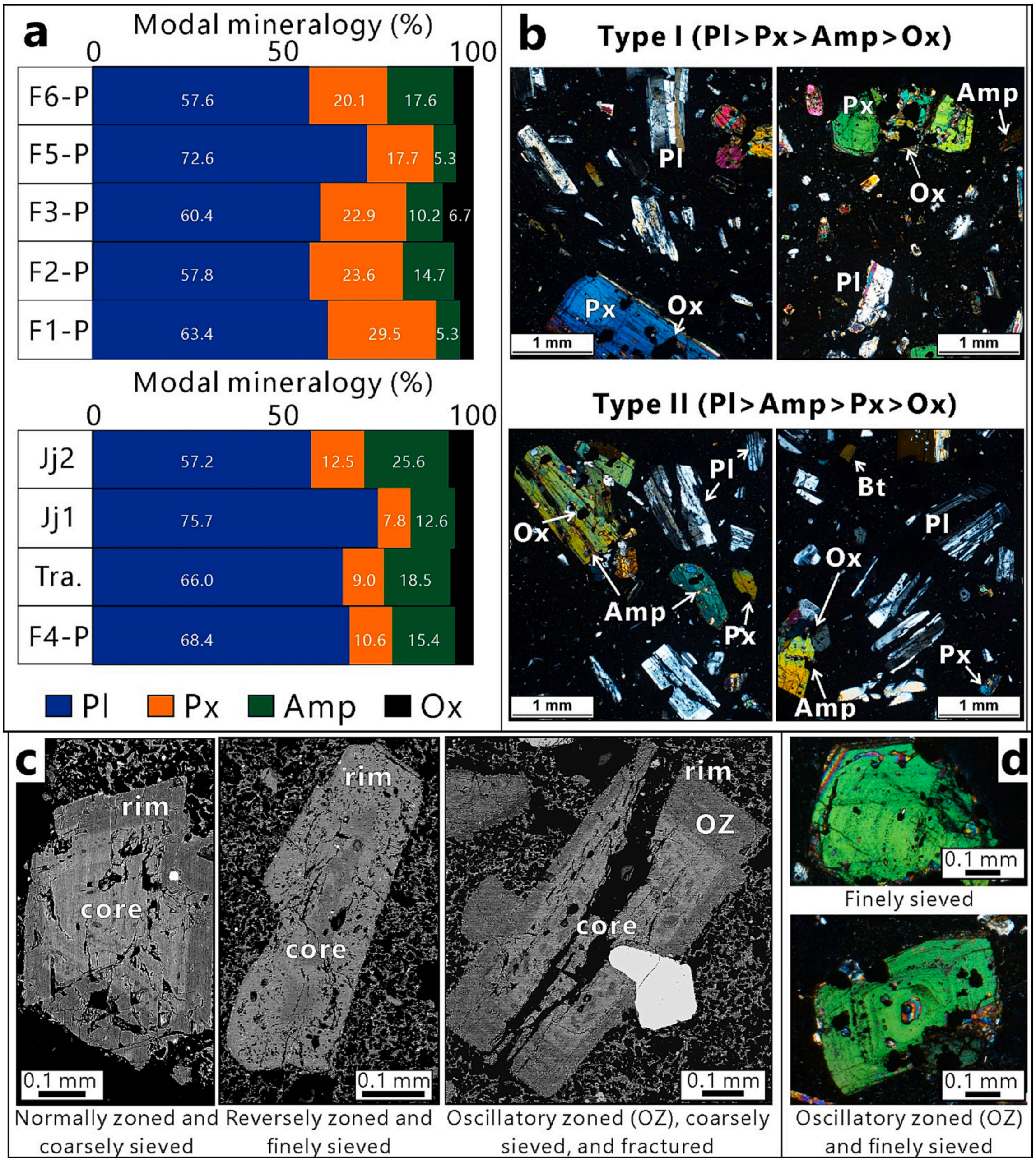

Fig. 5. (a) Modal mineralogy and petrographic images of the Young Merapi pumice fall deposits. All pumices include plagioclase (Pl), pyroxene (Px), amphibole (Amp) and oxides (Ox) as the main phenocryst phases. Numbers in the componentry column represents modal abundance of each respective mineral. (b) However, two types were observed based on the pyroxene abundances: the pyroxene-rich (type I) and the pyroxene-poor (type II). Note that many phenocrysts are fractured. (c) Representative BSE images of plagioclase phenocrysts showing three zoning variations: normal, reverse, and oscillatory (OZ). All zoning types often include fine and coarse sieve-textures. (d) Representative petrographic images of pyroxene showing the occurrence of fine sieve-texture and oscillatory zoning.

following the methods of Higgins (2002). Finally, the microlite number density (MND) were obtained from equations below:

$$MND\ (N_V) = (N_{AM}/D_M) \tag{4}$$

where N_{AM} is number density per unit area of microlite, and D_M is the average microlite diameter.

4. Results

4.1. Stratigraphy

From the composite stratigraphy of the studied locations, we observed nine pumice fall deposits from the product of the Young period (<2.2 ka–1,786 CE; hereafter referred as the Young Merapi). Note that we did not study the 1872 and 2010 CE eruptions because both episodes correspond to the Modern period (younger than 1,786 CE).

4.1.1. LOC 1

LOC 1 is a ± 180 cm-thick outcrop consisting of 5 pumice fall layers (F—P) intercalated with a brown layer from PDC (Figs. 2a-d, 3). Starting from the bottom, the first pumice fall layer (F1—P) is a ~ 6 cm-thick and massive, characterized by abundant lithics, and dominated by fine clast sizes (mostly 0.2–0.4 cm) (Fig. 2a, b). Going upward, the ~9 cm-thick second pumice fall (F2—P) is massive, with a significant decrease in lithic portions (lithic-poor) and no remarkable change in clast size (mostly between 0.2 and 0.4 cm). The third layer (F3—P) is a ~ 12 cm-

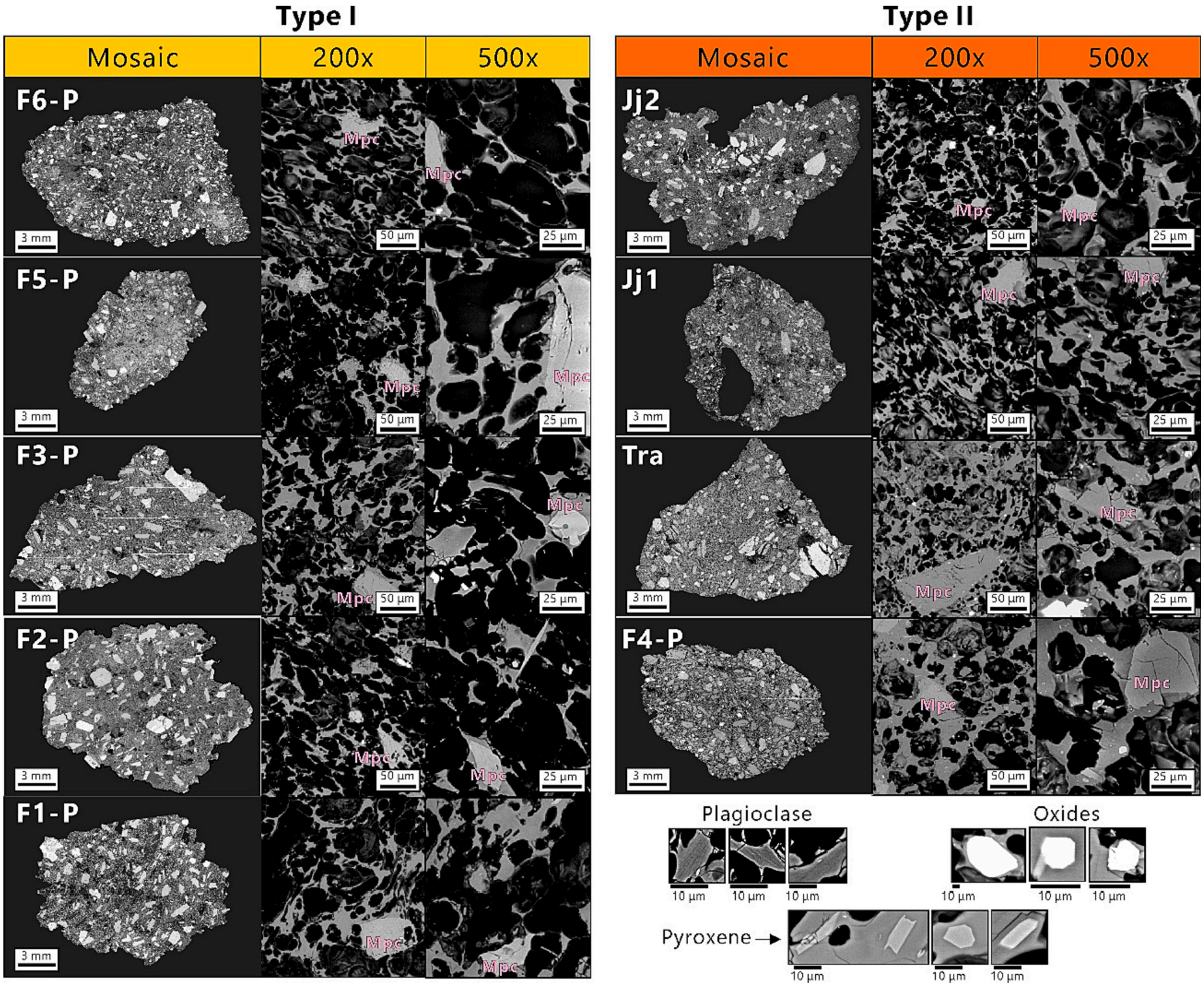

Fig. 6. Representative BSE images of Young Merapi pumice fall samples observed from mosaic, 200×, and 500×, magnifications. Note that type I pumice shows a relatively more vesiculated (i.e., larger matrix-vesicle size and more extensive coalescence) groundmass with less microlite fraction compared to type II pumice. Mpc denotes microphenocryst.

thick, massive and lithic-poor pumice fall layer, with typically larger clast sizes compared to the first and second pumice fall layers (mostly ~2 cm) (Fig. 2a, c). The fourth pumice fall layer (F4—P) corresponds to ~18 cm-thick massive deposit, with identical clast sizes to F3—P (mostly ~2 cm), and is characterized by the relatively low lithic content with respect to the previously described pumice fall layers (Fig. 2a, d). Due to a lack of detailed description from previous studies, we cannot correlate any of those four layers with the existing data (i.e., Andreastuti et al., 2000; Newhall et al., 2000; Gertisser et al., 2012). The uppermost layer at LOC 1 is~45 cm-thick and characterized by an internal stratification, with 4 sub-layers of fall deposits (from the lower to the upper part): a 20 cm-thick lower pumice (LP) lapilli, a 4 cm-thick grey ash (GA), an 11 cm-thick upper pumice (UP) lapilli, and a 10 cm-thick reddish ash (RA). All of these sub-layers are considerably lithic-rich (Fig. 2a, d). Due to the similarity in sedimentological, stratigraphical, and lithological features, we considered as the equivalent of the Trayem deposit described by Gertisser et al. (2012); (see their Fig. 11), with an estimated age of 1047 ± 37 cal. BP. Afterward, we named the pumice lapilli sub-units as Trayem lower pumice fall and Trayem upper pumice fall (Tra-LP and Tra-UP, respectively) (Fig. 2a, d), whereas the sub-unit ash layers are named as Trayem grey ash and Trayem reddish ash (Tra-GA and Tra-RA, respectively) (Fig. 2a, d).

4.1.2. *LOC 2*

LOC 2 is a ~ 220 cm-thick deposit which consists of 4 observable pumice fall layers (Figs. 2e, 3). The lowest layer was correlated with F4—P which was previously described at LOC 1 (Fig. 3); it is a massive, coarse (dominated by ~1.8 cm clasts), and lithic-poor pumice fall layer (Fig. 2e), with a thickness of ~9 cm. The second fall layer corresponds to the Trayem deposit (±50 cm), characterized by internal stratification of four sub-layers (Tra-LP, Tra-GA, Tra-UP, Tra-RA) (Figs. 2e-f, 3). At LOC 2, the thickness of Tra-UP is thinner, and the Tra-RA is significantly thicker than that observed at LOC 1 (~16 and 20 cm, respectively) (Figs. 2f, 3). Going upward, there is a ~ 7 cm-thick lithic-poor and fine-grained (mostly 0.2–0.4 cm) pumice fall deposit (F5—P), which underlines by a reddish ash layer (F5-RA) (Fig. 2e, g). Unlike the other pumice fall layer, F5—P contains scoriaeous juvenile material (Fig. 2g). The fourth pumice fall layer (the uppermost layer at LOC 2) consists of a ~ 11 cm-thick, massive, coarse (apparently dominated by ~3 cm clast size, but also rich in ~0.4 cm clasts), and lithic-rich pumice fall deposit, which underlines by a ~ 7–11 cm-thick grey ash layer. Because this deposit shows significant similarities with the Jurangjero 1 deposit of Gertisser et al. (2012); (see their Fig. 11), we refer to this layer as Jurangjero 1 (Jj1-P and Jj1-GA for the pumiceous and grey ash layer, respectively), dated at 762 ± 26 cal. BP (Gertisser et al., 2012) (Fig. 3).

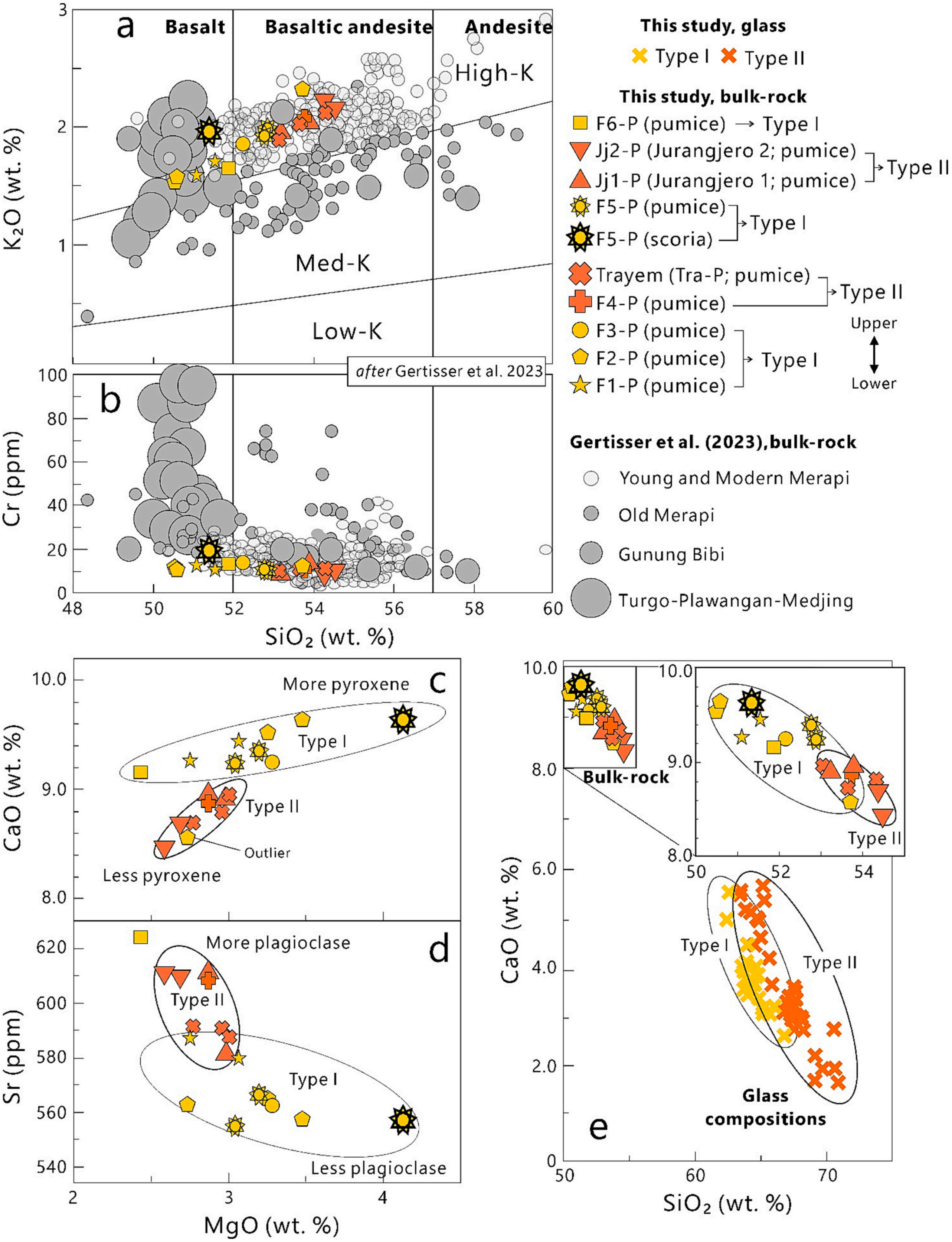

Fig. 7. Bivariate plots using some representative major and trace elements of Merapi samples. (a, b) We confirm that our samples (including pumice and scoria) belong to the Young Merapi stage, as indicated by the High-K (HK) affinity and low chromium (Cr) content (after Gertisser et al., 2023). (c, d,) Two geochemical patterns (specifically for CaO and Sr) were observed, and interestingly, this evidence agrees well with the definition of type I and II from petrographic observation; type I being more mafic (higher CaO, and lower SiO_2 and SrO) than type II. (e) Comparison of bulk-rock and glass chemical compositions of SiO_2 and CaO between type I and II pumices. All values have been normalized to 100 wt% (volatile-free).

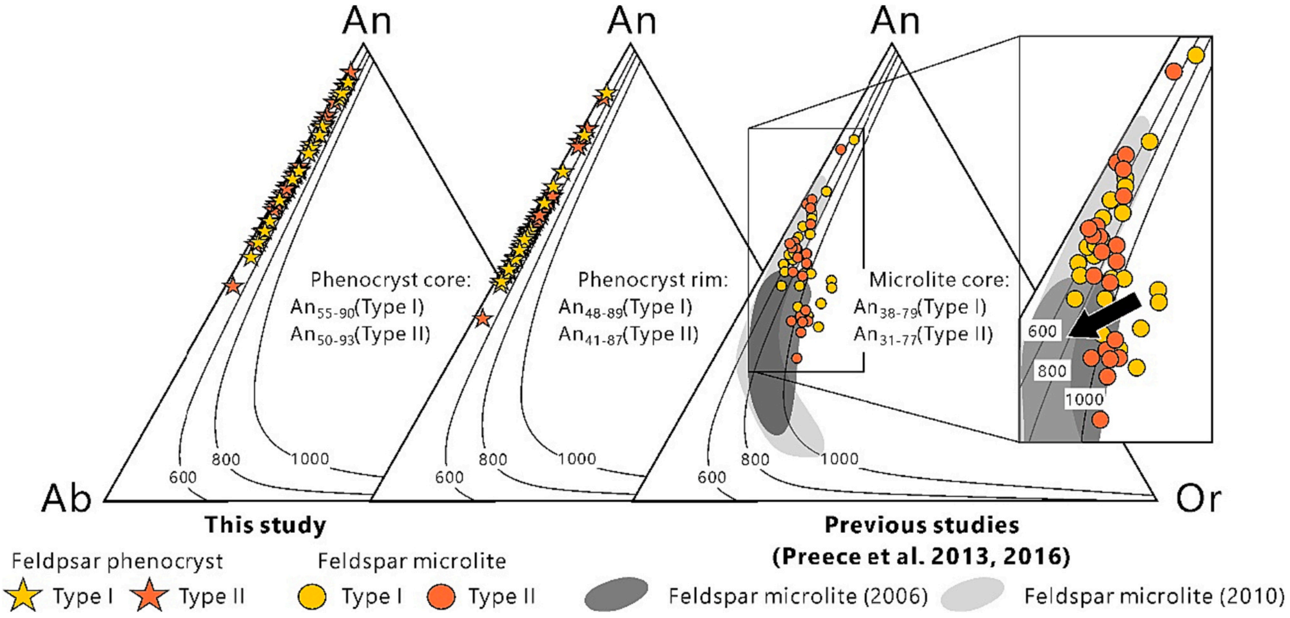

Fig. 8. Ternary feldspar diagram of Young Merapi pumice falls for feldspar phenocryst core (left), rim (middle), and feldspar microlite (right). Isothermal sections (i.e., magma temperature) of the dry ternary solvus was adapted from Preece et al., 2016, using VOLCALC (Wen and Nekvasil, 1994). Both pumice type shares relatively similar feldspar phenocryst core compositions ($An_{55–90}$ for type I and $An_{50–93}$ for type II). However, note type I has slightly more calcic feldspar phenocryst rim ($An_{48–89}$ for type I and $An_{41–87}$ for type II) and microlite ($An_{38–79}$ for type I and $An_{1–77}$ for type II) compositions than type II.

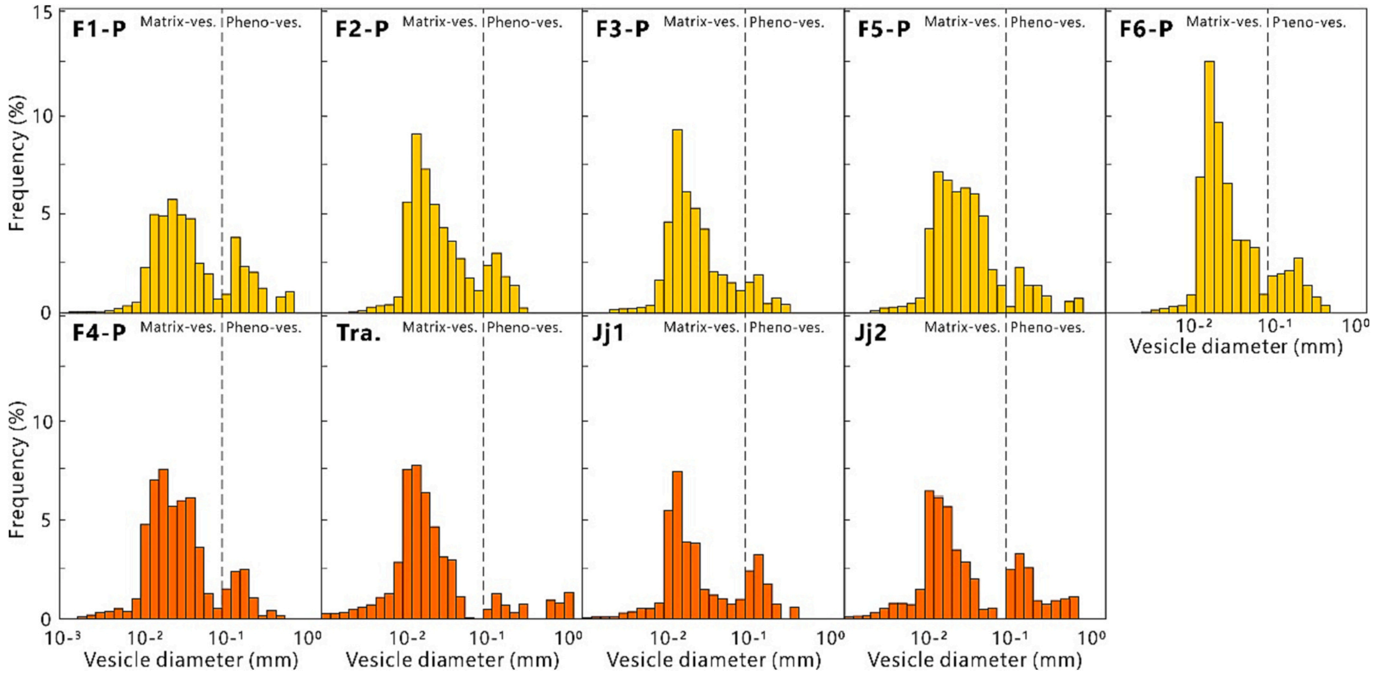

Fig. 9. 2D-vesicle size distributions (VSDs) of the Young Merapi pumice fall deposits. Yellow histogram denotes type I pumice, while orange histogram represents type II pumice. All pumices displayed bimodal vesicle populations with consistent boundary between pheno- and matrix-vesicles, at approximately 0.1 mm vesicle diameter. (For interpretation of the references to colour in this figure legend, the reader is referred to the web version of this article.)

4.1.3. LOC 3

LOC 3 preserves a relatively thin outcrop (~55 cm), consisting of two pumice fall layers (Figs. 2h-j, 3). The first layer (from the bottom) is a ~ 11 cm-thick, massive, coarse (mostly ~1 cm clast size, but also rich in ~0.4 cm clasts), and lithic-rich pumice fall deposit, which underlines by grey ash layer. This layer is easily correlable to the Jurangjero 1 eruption, which was previously described at LOC 2 (Fig. 3). The second pumice fall layer shows inner stratification in four sub-layers, including a lower pumice lapilli and a lower grey ash (which together totalize <1.5 cm of thickness), an upper pumice lapilli (~16 cm) and upper grey ash (~10 cm) (Fig. 2h). All sub-layers include abundant lithic clasts, and the mode of the grain size distribution is approximately 3 cm in diameter (Fig. 2j). Such features suggest a correlation between this pumice fall layer with the Jurangjero 2 deposit described by Gertisser et al. (2012), dated at 385 ± 65 cal. BP (see their Fig. 11). Thus, we named the second layer at LOC 3 as Jurangjero 2, and the sub-layers are labelled as Jj2-LP, Jj2-LGA, Jj2-UP, and Jj2-UGA, representing Jurangjero 2 lower pumice lapilli, lower grey ash, upper pumice lapilli, and upper grey ash,

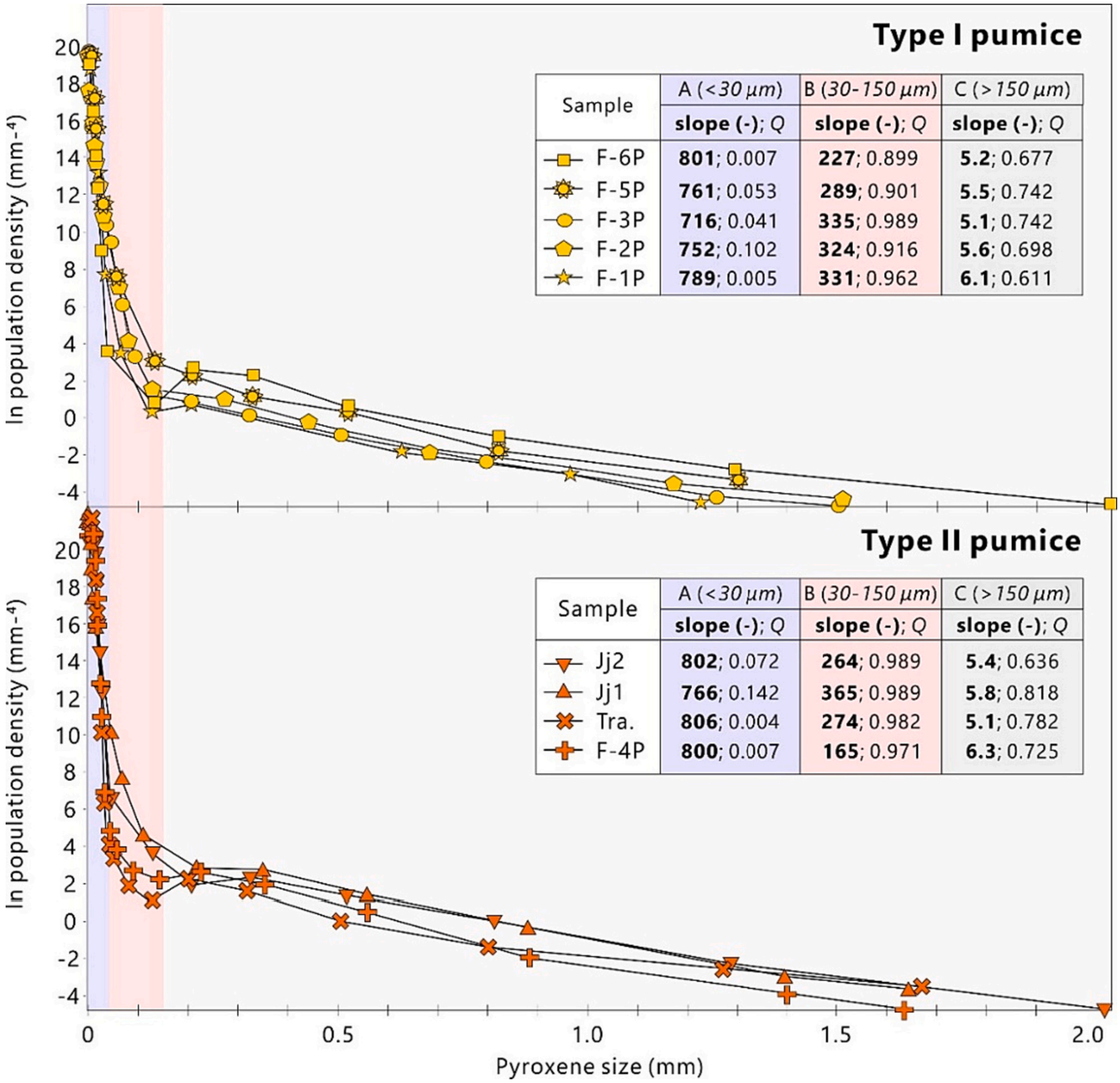

Fig. 10. Pyroxene crystal size distribution (CSD) of the Young Merapi pumice fall deposits. Based on the CSD slope variations (shown as A, B, and C), we define microlite, microphenocryst, and phenocryst as crystals with <0.03, 0.03–0.15, and > 0.15 mm diameter, respectively.

respectively (Figs. 2 and 3).

4.1.4. LOC 4

LOC 4 is a ± 120 cm-thick outcrop that includes a single pumice lapilli deposit (Fig. 2k and l). The 30 cm-thick pumice lapilli layer is massive and rich in fine-grained clasts (mostly 0.2–0.4 cm) and lithics. Such features make us unable to perform stratigraphic correlation with deposits at the other studied localities (LOC 1, 2, and 3). To solve this issue, we consulted the stratigraphy data of Newhall et al. (2000) and use the overlying black ash (BA) as a stratigraphic marker (Figs. 2l and 3). We suggest that this pumice lapilli deposit corresponds to an unnamed tephra unit at section I-Kali Krasak (Newhall et al., 2000; see their Fig. 4) due to its relative position to black ash (i.e., the unnamed tephra is just below the black ash) and similarity in the variation of clast sizes. Thus, we tend to name this unit as F6—P. Because the overlying PDC deposits have an estimated age of 250 ± 100 cal. BP (Newhall et al., 2000; see their Fig. 4) and show no correlation with western tephra deposits (the youngest tephra in the western flank is Jurangjero 2), we suggest that the F6—P layer must be younger than 250 ± 100 cal. BP, but older than 385 ± 65 cal. BP (Fig. 3).

4.2. Componentry variation

The Young Merapi pumice fall deposits comprise four main component types: pumice and/or scoria, lithics, and free crystals. Pumice clasts (brownish grey) are predominantly dense (i.e., low vesicularity); however, some highly vesicular and moderately vesicular pumices are also present in all layers (top to upper middle part of Fig. 4a). Unlike pumice, all scoria clasts are typically black and poorly vesicular (i.e., no occurrence of highly and/or moderately vesicular scoria) (Fig. 4b). Most of the lithics are fresh (grey to black) and displayed porphyritic texture with abundant phenocrysts (bottom middle part of Fig. 4a). The free crystals mainly include two mineral types, i.e., plagioclase and pyroxene (bottom part of Fig. 4a). The componentry data are reported as a number fraction, where the total number of each component type was divided by the total number of counted grains (e.g., Suhendro et al., 2022; Bunga Naen et al., 2023). The number fractions are labelled as C_{pumice}, C_{scoria}, $C_{lithics}$, and $C_{crystals}$ for pumice, scoria, lithics, and free crystals, respectively (Table 1).

Pumice and lithic clasts are negatively correlated and considered as the most dominant fraction on all deposits, varying from 50 to 89% for

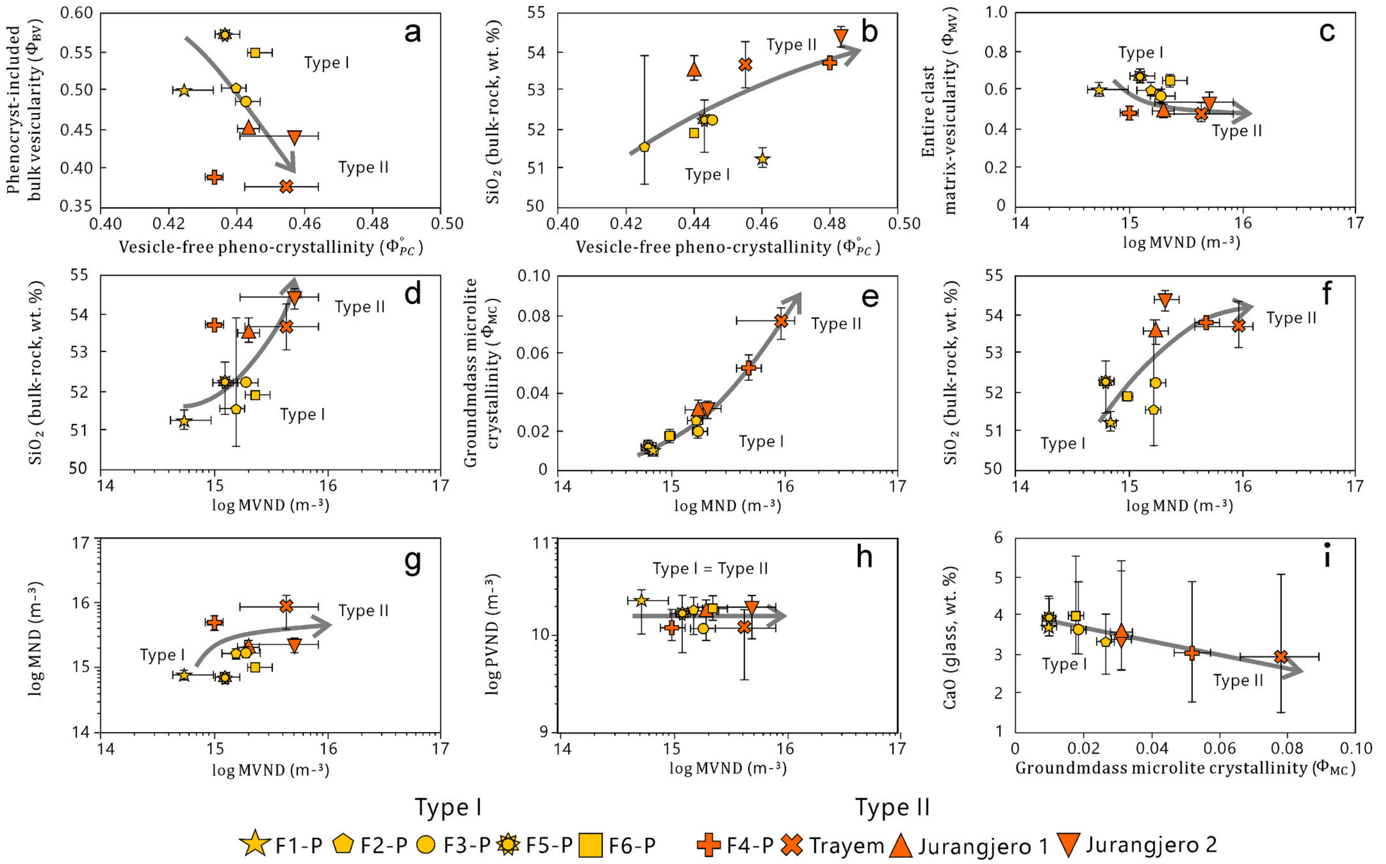

Fig. 11. Correlation of some important textural parameters. (a, b) Vesicle-free pheno-crystallinity (Φ_{PC}°) is found to be negatively and positively correlated with bulk-vesicularity (Φ_{BV}) and bulk-rock silica content. (c, d) Matrix-vesicle number density (MVND) shows negative and positive correlation with matrix-vesicularity (Φ_{MV}) and bulk-rock silica content. (e, f) Microlite number density (MND) is positively correlated with microlite fraction (Φ_{MC}) and bulk-rock silica content. (g) Positive correlation between MVND and MND. (h) Constant correlation between MVND and PVND. (i) Negative correlation between Φ_{MC} and CaO_{glass}.

Table 1

Componentry result of the Young Merapi pumice fall deposits. *C* is the number fraction of each component type, obtained by dividing the number of each component type with the summation of counted clasts for each unit (n / n_{tot}).

Pumice fall layer	Number of pumices within each class (mm)				Number of scoriae within each class (mm)				Number of lithics within each class (mm)				Number of free crystals within each class (mm)				Total number of clasts (n_{tot})
	> 32	16–32	8–16	4-8	> 32	16–32	8–16	4-8	> 32	16–32	8–16	4-8	> 32	16–32	8–16	4-8	
F1-P	1	2	28	125	0	0	0	0	0	0	10	94	0	0	0	0	260
	n (*C*$_{pumice}$): 156 (60.0)				**n (*C*$_{scoria}$):** 0 (0)				**n (*C*$_{lithic}$):** 104 (40.0)				**n (*C*$_{crystal}$):** 0 (0)				
F2-P	1	2	37	246	0	0	0	0	0	1	1	51	0	0	0	0	339
	Total pumice: 286 (84.4)				**n (*C*$_{scoria}$):** 0 (0)				**n (*C*$_{lithic}$):** 53 (15.6)				**n (*C*$_{crystal}$):** 0 (0)				
F3-P	1	5	48	348	0	0	0	0	0	3	16	71	0	0	0	0	492
	n (*C*$_{pumice}$): 402 (81.7)				**n (*C*$_{scoria}$):** 0 (0)				**n (*C*$_{lithic}$):** 90 (18.3)				**n (*C*$_{crystal}$):** 0 (0)				
F4-P	4	3	46	92	0	0	0	0	0	0	2	16	0	0	0	0	166
	n (*C*$_{pumice}$): 148 (89.2)				**n (*C*$_{scoria}$):** 0 (0)				**n (*C*$_{lithic}$):** 18 (10.8)				**n (*C*$_{crystal}$):** 0 (0)				
Tra-LP	2	8	46	415	0	0	0	0	2	2	29	283	0	0	0	7	794
	n (*C*$_{pumice}$): 471 (59.2)				**n (*C*$_{scoria}$):** 0 (0)				**n (*C*$_{lithic}$):** 316 (39.8)				**n (*C*$_{crystal}$):** 7 (0.8)				
Tra-UP	0	0	34	208	0	0	0	0	0	0	15	229	0	0	0	2	488
	n (*C*$_{pumice}$): 242 (49.6)				**n (*C*$_{scoria}$):** 0 (0)				**n (*C*$_{lithic}$):** 244 (49.6)				**n (*C*$_{crystal}$):** 2 (0.4)				
F5-P	0	3	11	125	0	0	5	53	0	1	4	40	0	0	0	2	243
	n (*C*$_{pumice}$): 139 (57.2)				**n (*C*$_{scoria}$):** 58 (23.9)				**n (*C*$_{lithic}$):** 45 (18.5)				**n (*C*$_{crystal}$):** 1 (0.4)				
Jj1-P	1	6	12	78	0	0	0	0	0	1	4	30	0	0	0	0	133
	n (*C*$_{pumice}$): 98 (73.5)				**n (*C*$_{scoria}$):** 0 (0)				**n (*C*$_{lithic}$):** 35 (26.5)				**n (*C*$_{crystal}$):** 0 (0)				
Jj2-LP	1	7	22	216	0	0	0	0	0	0	6	122	0	0	0	4	374
	n (*C*$_{pumice}$): 242 (64.7)				**n (*C*$_{scoria}$):** 0 (0)				**n (*C*$_{lithic}$):** 128 (34.2)				**n (*C*$_{crystal}$):** 4 (1.0)				
Jj2-UP	3	3	16	149	0	0	0	0	0	1	6	91	0	0	0	2	271
	n (*C*$_{pumice}$): 171 (63.2)				**n (*C*$_{scoria}$):** 0 (0)				**n (*C*$_{lithic}$):** 98 (36.1)				**n (*C*$_{crystal}$):** 2 (0.7)				
F6-P	2	11	40	345	0	0	0	0	1	0	27	222	0	0	0	14	662
	n (*C*$_{pumice}$): 398 (59.7)				**n (*C*$_{scoria}$):** 0 (0)				**n (*C*$_{lithic}$):** 250 (31.6)				**n (*C*$_{crystal}$):** 14 (2.3)				

C_{pumice} and 11 to 50% for C_{lithic} (Fig. 4c). Interestingly, there is the tendency for the thicker deposits to include higher lithic portions than those of thinner deposits (Fig. 4c). In particular, lithic portions in deposits with <20 cm thickness (except F1—P) such as F2—P, F3—P, F4—P, F5—P, and Jurangjero 1 vary from 11 to 26.5% (Figs. 3 and 4). While the relatively thick deposits (>20 cm) such as Trayem, Jurangjero 2, and F6—P comprise higher lithic contents, ranging from 31.6 to 49.6% (Figs. 3 and 4). Scoria clast is only present in the F5—P, with a relatively high abundance (C_{scoria} = 23.9%). Free crystals were observed only in the Trayem, F5—P, Jurangjero 2, and F6—P (specifically below 8 mm grains); however, their abundance was considerably low (0.4–2.3%) (Table 1).

4.3. Petrography

A summary of the petrographic observation is listed in Table 2. All studied pumices include plagioclase (Pl), pyroxene (Px), amphibole (Amp), and oxides (Ox) as the main phenocryst phases. Biotite (Bt) and apatite (Ap) were also observed, but their relative abundances are lower than 0.5% (Fig. 5a, b). Plagioclase and pyroxene phenocrysts from all samples were predominantly zoned (including normal, reverse, and oscillatory zoning textures), sieved (coarse and fine), and fractured (especially for larger phenocrysts) (Fig. 5b, c). By contrast, amphibole, biotite, oxides, and apatite phenocrysts displayed un-zoned texture with minimum fractures (Fig. 5b). Based on the relative abundance of pyroxene, we suggested two different types of pumice: the pyroxene-rich (type I, where the relative abundance of pyroxene reached >15%) and the pyroxene-poor (type II, where the relative abundance of pyroxene is <15%) (Fig. 5a). Type I was found exclusively in F1—P, F2—P, F3—P, F5—P, and F6—P layers, while Type II characterizes F4—P, Trayem, Jurangjero 1, and Jurangjero 2 layers (Fig. 5a).

Crystals in the groundmass glass (including microlite and microphenocryst) consist of three mineral phases: plagioclase, pyroxene, and oxides (Fig. 6). Both plagioclase and pyroxene displayed zoned (normal and reverse) and un-zoned textures, while oxides were typically unzoned. Unlike phenocrysts, no sieved and oscillatory zoning textures were observed in the groundmass crystals (Fig. 6).

Table 2
Summary of petrography of the Young Merapi pumice fall deposits.

Pumice fall layer	Phenocrysts phase	Textures (O: present, X: absent)						Vesicle-free phenocrystallinity (φ°_{PC})	Modal mineralogy (%)
		Un-zoned	Normally zoned	Reversely zoned	Oscillatory zoned	Sieved (Coarse and fine)	Fractured		
F1-P	Pl	O	O	O	O	O	O	0.290	63.44
	Px	O	O	O	O	O	X	0.135	29.54
	Amp	O	X	X	X	X	X	0.025	5.26
	Ox	O	X	X	X	X	X	0.008	1.76
	All							0.459	100.00
F2-P	Pl	O	O	O	O	O	O	0.244	57.82
	Px	O	O	O	O	O	O	0.101	23.63
	Amp	O	X	X	X	X	O	0.062	14.69
	Ox	O	X	X	X	X	X	0.015	3.55
	All							0.422	100.00
F3-P	Pl	O	O	O	O	O	O	0.270	60.43
	Px	O	O	O	O	O	X	0.102	22.87
	Amp	O	X	X	X	X	X	0.045	10.02
	Ox	O	X	X	X	X	X	0.029	6.68
	All							0.445	100.00
F4-P	Pl	O	O	O	O	O	O	0.329	68.40
	Px	O	O	O	O	O	O	0.051	10.60
	Amp	O	X	X	X	X	X	0.074	15.39
	Ox	O	X	X	X	X	X	0.027	5.61
	All							0.481	100.00
Trayem (Tra-LP and Tra-UP)	Pl	O	O	O	O	O	O	0.303	66.02
	Px	O	O	O	O	O	O	0.041	8.98
	Amp	O	X	X	X	X	O	0.085	18.45
	Ox	O	X	X	X	X	X	0.030	6.55
	All							0.459	100.00
F5-P	Pl	O	O	O	O	O	O	0.291	72.57
	Px	O	O	O	O	O	X	0.071	17.69
	Amp	O	X	X	X	X	X	0.021	5.31
	Ox	O	X	X	X	X	X	0.018	4.43
	All							0.445	100.00
Jurangjero I (Jj1-P)	Pl	O	O	O	O	O	O	0.333	75.67
	Px	O	O	O	O	O	O	0.034	7.77
	Amp	O	X	X	X	X	O	0.054	12.16
	Ox	O	X	X	X	X	X	0.019	4.39
	All							0.440	100.00
Jurangjero II (Jj2-LP and Jj2-UP)	Pl	O	O	O	O	O	O	0.278	57.16
	Px	O	O	O	O	O	O	0.060	12.45
	Amp	O	X	X	X	X	O	0.124	25.63
	Ox	O	X	X	X	X	X	0.023	4.76
	All							0.485	100.00
F6-P	Pl	O	O	O	O	O	O	0.255	57.56
	Px	O	O	O	O	O	O	0.089	20.09
	Amp	O	X	X	X	X	X	0.078	17.61
	Ox	O	X	X	X	X	X	0.021	4.74
	All							0.443	100.00

Table 3
Bulk-rock chemical analysis of Young Merapi pumice samples. All samples are in wt% and normalized to 100% (volatile-free).

Sample:	F1-P	F1-P	F2-P	F2-P	F2-P	F3-P	F4-P	Tra-LP	Tra-LP	Tra-UP
	Pumice	Pumice	Pumice	Pumice	Pumice	Pumice	Pumice	Pumice	Pumice	Pumice
SiO_2	51.66	51.28	50.67	53.86	50.66	52.20	53.86	53.79	53.26	54.42
TiO_2	0.91	0.89	0.99	0.83	0.98	0.92	0.77	0.79	0.75	0.77
Al_2O_3	20.19	21.44	20.69	19.05	20.33	19.65	19.17	19.52	19.67	18.80
MnO	0.21	0.19	0.19	0.20	0.20	0.19	0.20	0.19	0.20	0.19
MgO	3.08	2.78	3.26	2.73	3.48	3.30	2.89	2.77	3.00	2.98
CaO	9.48	9.23	9.56	8.59	9.67	9.24	8.91	8.71	8.99	8.77
Na_2O	2.99	2.92	2.82	3.48	2.87	3.04	3.26	3.28	3.15	3.31
K_2O	1.69	1.60	1.55	2.31	1.56	1.87	2.07	2.02	1.91	2.13
P_2O_5	0.31	0.37	0.29	0.26	0.26	0.26	0.29	0.31	0.32	0.28
Fe_2O_3	9.48	9.32	9.98	8.69	9.99	9.31	8.59	8.60	8.74	8.32
Total	100.00	100.00	100.00	100.00	100.00	100.00	100.00	100.00	100.00	100.00
ppm										
V	201	271	428	371	476	254	296	267	252	236
Cr	12	14	11	12	9	15	14	10	11	21
Ni	11	13	8	15	2	6	4	10	6	16
Rb	35	31	30	48	30	36	46	46	42	49
Sr	581	586	563	562	555	562	609	590	589	589
Y	20	20	21	21	20	21	21	20	20	20
Zr	111	119	115	104	113	107	112	117	121	111
Nb	0	5	0	7	0	1	4	4	1	4
Ba	313	356	395	593	470	392	503	468	482	350

Sample:	F5-P	F5-P	F5-P	Jj1-P	Jj1-P	Jj2-LP	Jj2-UP	F6-P
	Scoria	Pumice	Pumice	Pumice	Pumice	Pumice	Pumice	Pumice
SiO_2	51.41	52.89	53.05	53.6	53.36	54.62	54.49	51.96
TiO_2	0.95	0.86	0.84	0.77	0.81	0.71	0.74	0.82
Al_2O_3	18.00	18.95	18.92	18.92	19.61	19.43	19.14	21.71
MnO	0.23	0.22	0.21	0.20	0.20	0.20	0.20	0.19
MgO	4.14	3.21	3.06	2.99	2.89	2.60	2.68	2.45
CaO	9.63	9.38	9.28	8.91	8.87	8.46	8.73	9.18
Na_2O	2.98	3.15	2.99	3.24	3.18	3.33	3.38	3.09
K_2O	1.97	1.94	1.70	2.05	1.96	2.17	2.18	1.64
P_2O_5	0.31	0.29	0.31	0.31	0.32	0.30	0.29	0.33
Fe_2O_3	10.37	9.09	9.49	8.73	8.78	8.18	8.17	8.61
Total	100.00	100.00	100.00	100.00	100.00	100.00	100.00	100.00
ppm								
V	297	151	156	329	374	352	236	236
Cr	21	11	10	10	10	11	7	13
Ni	9	3	15	10	6	8	4	7
Rb	40	39	40	44	45	51	48	35
Sr	557	565	556	580	609	609	610	625
Y	20	22	21	21	20	20	22	21
Zr	104	109	111	113	117	117	111	123
Nb	15	8	5	3	7	6	4	1
Ba	293	396	282	487	445	617	507	376

Table 4
Average groundmass glass chemical compositions of type I and type II pumices. All samples are in wt% and normalized to 100%.

Sample:	Type I pumice ($n = 25$)	Type II pumice ($n = 35$)
SiO_2	64.31 (±2.23)	67.01 (±7.13)
TiO_2	0.58 (±0.02)	0.38 (±0.01)
Al_2O_3	17.71 (±1.99)	18.09 (±3.81)
MnO	0.20 (±0.01)	0.14 (±0.01)
MgO	1.28 (±0.12)	0.74 (±0.20)
CaO	3.69 (±1.04)	3.47 (±2.04)
Na_2O	3.41 (±0.48)	3.21 (±1.24)
K_2O	4.40 (±0.64)	4.00 (±0.86)
FeOtot.	4.39 (±0.71)	2.89 (±0.67)
Total	100.00	100.00

4.4. Bulk-rock, glass, and feldspar phenocryst and microlite compositions

The representative bulk-rocks and glasses compositions are listed in Tables 3 and 4, respectively. We confirm that our samples belong to the Young Merapi stage (<2.2 ka–1,786 CE; Gertisser et al., 2012), as shown by the high-K (HK) and low chromium (Cr) characteristics of bulk-rock chemical composition (Fig. 7a, b). Interestingly, type I also shows a distinctive bulk-rock and glass chemical pattern compared to Type II, specifically for silica, calcium, and strontium contents (Fig. 7c-e). In particular, type I is classified as basalt to basaltic andesite (50.5–53.7 wt% SiO_{2bulk}) with andesitic-dacitic glass (62.3–66.6 wt% SiO_{2glass}), rich in calcium (>9 wt% CaO_{bulk}) and poor in strontium (<580 ppm Sr_{bulk}). While type II is classified as basaltic andesite (53.2–54.5 wt% SiO_{2bulk}), having dacitic glass compositions (63.3–70.8 wt% SiO_{2glass}) with poor calcium (<9 wt% CaO_{bulk}) and abundant strontium (>580 ppm Sr_{bulk}). Most pumice fall layer is characterized by the homogeneous bulk-rock composition (i.e., <1 wt% difference in SiO_{2bulk} between each analyzed sample), except for F2—P and F5—P (Table 3). Both F2—P And F5—P show bimodal juvenile composition, that is, basalt and basaltic andesite. F2—P has the largest SiO_{2bulk} interval, i.e., >3 wt% difference in silica between basalt (50.66–50.67 wt% SiO_{2bulk}) and basaltic andesite (53.86 wt% SiO_{2bulk}). F5—P has a narrower SiO_{2bulk} interval than that of F2—P (~1.5 wt%); such variation was found to be related to the juvenile type, that is, scoria (51.41 wt% SiO_{2bulk}) and pumice (52.81–53.05 wt% SiO_{2bulk}) (Fig. 7a).

There is no remarkable difference in terms of feldspar phenocryst core composition between type I and II, as shown by the overlapping anorthite contents ($(An = Ca/(Ca + Na + K$; $An_{55–90}$ for type I and $An_{50–93}$ for type II) (Fig. 8). In contrast, feldspar phenocryst rim and microlite compositions show distinct differences, with type I being more calcic than type II ($An_{48–89}$ and $An_{38–79}$ for Type I, and $An_{41–87}$ and $An_{31–70}$ for Type II) (Fig. 8).

4.5. *Definition of vesicles and crystals*

The VSDs data showed that all pumices displayed bimodal vesicle populations, with the boundary between pheno- and matrix-vesicles occur at approximately 0.1 mm vesicle diameter (Fig. 9), similar to those of St. Helens, Crater Lake (Mazama), Novarupta, Santorini, Maninjau pumices (e.g., Klug and Cashman, 1994; Klug et al., 2002; Adams et al., 2006; Simmons et al., 2017; Suhendro et al., 2022).

Three slope variations were observed in pyroxene CSD data, both for type I and type II pumices (Fig. 10). The first slope (A) represents the steepest slope variation, ranging from −716 to −806. The second slope (B) is characterized by a relatively medium value, varying from −165 to −365. While the third slope (C) represents the gentlest slope, ranging from −6.3 to −5.1. Based on such slope characterizations, we define microlites, microphenocrysts, and phenocrysts as those crystals with <0.03, 0.03–0.15, and > 0.15 mm diameter, respectively (Fig. 10). Such crystal definitions are similar to those defined at Vesuvius, Lassen Peak, Unzen, Pinatubo, and Rabaul (e.g., Gurioli et al., 2005; Shea et al., 2009; Shea et al., 2012; Salisbury et al., 2008; Cichy et al., 2011; Hammer et al., 1999; Bernard and de Maisonneuve, 2020). Moreover, it is known that microphenocryst can be attributed to two different origins: (1) pre-eruptive crystallization via slow depressurization (just before the eruption; Shea et al., 2009), and (2) fragmented or broken phenocrysts (Pallister et al., 1996; van Zalinge et al., 2018). Therefore, to avoid such ambiguity, we neglect the discussion on microphenocryst; instead, we tend to focus on phenocryst and microlite.

4.6. *Correlation of textural properties*

Comparison of the representative BSE images of type I and II pumices are shown in Fig. 11. Type I and II pumices are considerably phenocryst-rich; however, Type I is found to be slightly less crystalline than type II (0.42–0.45 φ_{PC}° and 0.43–0.49 φ_{PC}°, respectively). Vesicle-free pheno-crystallinity is found to be negatively and positively correlated with bulk-vesicularity (φ_{BV}) and SiO_{2bulk}, respectively (Fig. 11a, b). Type I pumice has a higher range of both bulk- and matrix-vesicularity than Type II pumice (0.48–0.57 and 0.58–0.65, and 0.37–0.45 and 0.45–0.50, respectively) (Fig. 9c-f). For type I, the MVND vary from 0.6 × 10^{15} m^{-3} to 2.3 × 10^{15} m^{-3}, and the MND range from 0.7 × 10^{15} m^{-3} to 1.8 × 10^{15} m^{-3}, with 0.01–0.02 microlite crystallinity (φ_{MC}; i.e., fraction of microlites in the groundmass glass). For type II, the MVND vary from 1.0 × 10^{15} m^{-3} to 6.5 × 10^{15} m^{-3}, and the MND range from 1.8 × 10^{15} m^{-3} to 7.4 × 10^{15} m^{-3}, with 0.03–0.07 φ_{MC}. The MVND is negatively correlated with matrix-vesicularity (Fig. 11c), resulting in positive correlation with SiO_{2bulk} (Fig. 11d), whereas the MND shows positive correlation with microlite crystallinity (φ_M) and SiO_{2bulk} (Fig. 11e, f). Since both MVND and MND are positively correlated with bulk-rock silica content, MVND yield a positive correlation with MND (Fig. 11g). Both pumice types have nearly identical PVND values (1.0–3.1 × 10^{10} m^{-3}), with PVND showing no correlation with MVND (as well as MND) (Fig. 11h). Noteworthy, we also found that CaO_{glass} of both pumice types exhibit negative correlation with φ_{MC}. A summary of the textural parameters is listed in Table 5.

5. Discussion

5.1. *Magmatic origins and pre-eruptive conditions of type I and II pumices*

One indication of a similar magmatic source (co-magmatic origin) is the linear correlation (i.e., single trend) between all major and trace elements, such as those observed in the 90 ka eruption of Aso, the 39 ka eruption of Campi Flegrei, the 12 ka eruption of Laacher See, and the 1815 CE eruption of Tambora (e.g., Kaneko et al., 2007; Forni et al., 2016; Ginibre et al., 2004; Suhendro et al., 2021). However, in this Young Merapi case, we found two different bulk-rock geochemical trends (particularly between silica, magnesium, calcium, and strontium) (Fig. 7c, d) as well as two distinct phase assemblages, with type I and II pumice being pyroxene-rich and pyroxene-poor, respectively (Fig. 5a). Despite the difference, both pumice types have a relatively similar amphibole fractions and feldspar phenocryst rim compositions (the most evolved composition reached $An_{40–50}$). This suggest that both pumice types were sourced from different magmatic reservoirs with different crystallization histories, but stored at relatively similar water contents

Table 5

Textural parameter of the Young Merapi pumice samples. φ_{BV}, φ_{PC}, φ_{PV}, φ_{mv}, φ_{MV} and φ_M correspond to bulk-vesicularity, pheno-crystallinity, pheno-vesicularirty, high magnification (500×) matrix-vesicularity, entire clast matrix-vesicularity, and microlite crystallinity, respectively. The superscript “*” indicates phenocryst-free vesicularity, while the superscript “o” represents vesicle-free crystallinity. *D* indicates average diameter, while *Nv* represents number density for each given parameter.

Location, unit, pumice type	φ_{BV} (φ_{BV}^{*})	φ_{PC} (φ_{PC}°)	Pheno-vesicle			Matrix-vesicle				Microlite		
			D_{PV} (mm)	φ_{PV}^{*}	*PVND*, N_v (m^{-3})	D_{MV} (mm)	φ_{mv}	φ_{MV}	*MVND*, N_v (m^{-3})	D_M (mm)	φ_{MC}	*MND*, N_v (m^{-3})
F1-P (Type I)	0.50 (0.65)	0.23 (0.46)	0.18	0.32	3.1 × 10^{10}	0.006	0.58	0.37	0.6 × 10^{15}	0.002	0.01	0.7 × 10^{15}
F2-P (Type I)	0.51 (0.64)	0.21 (0.42)	0.22	0.23	1.9 × 10^{10}	0.009	0.59	0.42	1.8 × 10^{15}	0.002	0.02	1.7 × 10^{15}
F3-P (Type I)	0.45 (0.59)	0.29 (0.48)	0.21	0.10	1.2 × 10^{10}	0.009	0.58	0.42	2.1 × 10^{15}	0.002	0.02	1.8 × 10^{15}
F5-P (Type I)	0.57 (0.70)	0.19 (0.44)	0.26	0.23	1.5 × 10^{10}	0.008	0.67	0.49	1.4 × 10^{15}	0.002	0.01	0.7 × 10^{14}
F6-P (Type I)	0.55 (0.69)	0.20 (0.44)	0.23	0.25	2.1 × 10^{10}	0.010	0.65	0.47	2.3 × 10^{15}	0.003	0.02	0.9 × 10^{14}
F4-P (Type II)	0.38 (0.54)	0.29 (0.48)	0.26	0.16	1.2 × 10^{10}	0.009	0.49	0.32	1.0 × 10^{15}	0.002	0.05	4.8 × 10^{15}
Trayem (Type II)	0.37 (0.52)	0.29 (0.46)	0.25	0.15	1.3 × 10^{10}	0.006	0.47	0.31	5.1 × 10^{15}	0.002	0.07	7.4 × 10^{15}
Jurangjero I (Type II)	0.45 (0.54)	0.27 (0.44)	0.22	0.16	1.7 × 10^{10}	0.007	0.49	0.33	1.8 × 10^{15}	0.003	0.04	1.9 × 10^{15}
Jurangjero II (Type II)	0.43 (0.59)	0.27 (0.49)	0.19	0.23	2.4 × 10^{10}	0.005	0.54	0.31	6.5 × 10^{15}	0.002	0.03	2.2 × 10^{15}

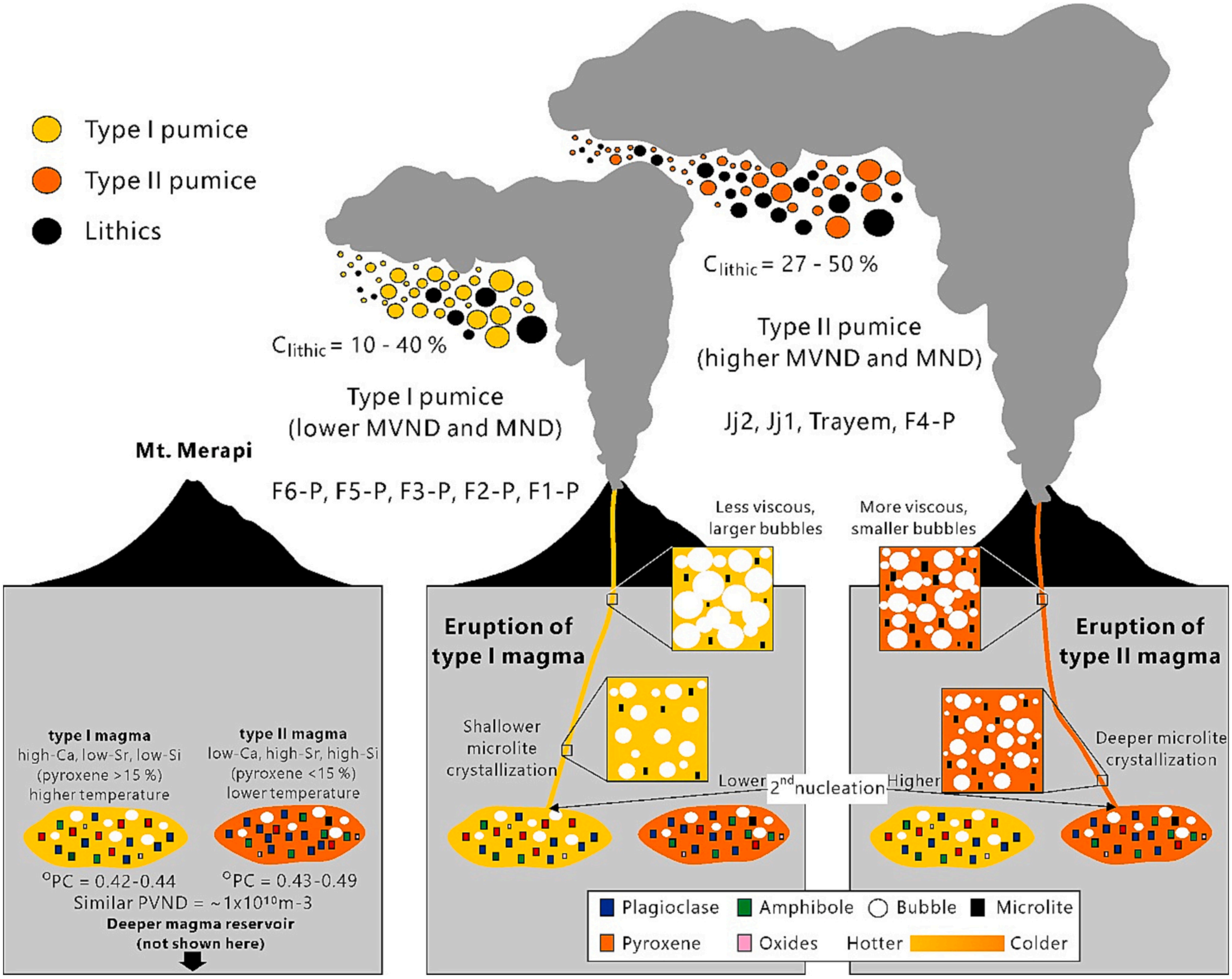

Fig. 12. Illustration showing the dynamics of pre- and *syn*-eruptive conditions of the Young Merapi pumice eruptions. The relatively similar bulk-rock composition, coupled with the relatively similar amphibole content and PVNDs value may suggest that type I and II magmas were stored at relatively similar pressure (depth). When eruption occurs, the cold-more evolved type II magma will experience more extensive matrix-bubble nucleation and deeper microlite crystallization than the hot-less evolved type I magma. As the MVND and MND increase, magma decompression rate and viscosity increase, allowing type II magma to erupt more explosively than type I (i.e., higher eruption plume and more dispersed fall area).

(~4–6 wt%) and storage pressure (~200 MPa) (Costa et al., 2013; Innocenti et al., 2013) (hereafter referred as to type I magma and type II magma, respectively) (Fig. 12). In particular, although type I includes significantly higher modal abundance of pyroxene (Fig. 5a), the glass composition of silica and calcium remains slightly lower and higher than type II, respectively (Fig. 7e). Since magmatic differentiation (represented by the increasing trend of silica content or decreasing magnesium in residual melt; e.g., Turner et al., 2003, Handley et al., 2007) is a result of crystallization of mafic minerals in a cooling magma (McBirney, 2007), we can expect that the starting composition of type I magma must be more primitive (i.e., lower SiO_2 and higher CaO) than type II magma, thus facilitating more extensive pyroxene crystallization with less plagioclase (i.e., higher pyroxene fractionation reduces the modal abundance of plagioclase; Fig. 5a) (Handley et al., 2007). Finally, because pyroxene is one of primary silicate minerals that includes abundant calcium and/or magnesium (McBirney, 2007), and strontium can substitute for calcium during the crystallization of calcic plagioclase (Cherniak and Watson, 1994), the bulk-rock composition of type I yields higher calcium (CaO_{bulk}) and magnesium (MgO_{bulk}), and lower strontium (Sr_{bulk}) contents compared to type II (Fig. 7c).

Phenocryst rim and microlite composition record late-stage crystallization in magmas, hence their compositions reflect the final physiochemical conditions of magma prior to eruption (Hammer et al., 1999; Toramaru, 2019; Suhendro et al., 2021). Therefore, because type I pumice include a slightly more calcic feldspar rim and microlite compositions than type II pumice, and higher magmatic temperatures result in more anorthitic feldspars (Couch et al., 2003), we suggest that type I magma was hotter than type II magma (Fig. 8). This supports our idea that type I pumice originates from a more primitive magmatic source than type II pumice, and shows good agreement with the general idea that a lower SiO_2 magma corresponds to a higher magma temperature and vice versa (Toramaru, 2006; Ridolfi and Renzulli, 2012), with type I being slightly less evolved than type II (50.5–53.7 wt% SiO_{2bulk} and 53.2–54.5 wt% SiO_{2bulk}, respectively) (Fig. 7). Moreover, the fact that type II pumice include slightly more abundant pheno-crystallinity than type I (Fig. 11a, b) imply that type II magma experienced more extensive cooling process, which led to more significant phenocryst crystallization. Thus, we suggest that type I and II magmas had similar rate of overpressures prior to eruption, as indicated by PVND values (Fig. 11h). Such PVNDs are similar to the other VEI 3–5 eruptions that did not form calderas ($\pm1.0 \times 10^{10}$ m^{-3}), but significantly lower than the VEI 6–8 caldera-forming eruptions ($\pm1.0 \times 10^{11}$ m^{-3}) (Suhendro et al., 2022, Suhendro and Toramaru in prep.).

Finally, the fact that both pumice types have abundant disequilibrium textures (i.e., finely sieved and reversely and oscillatory zoned; Fig. 5b-d) in plagioclase and pyroxene phenocrysts suggests that both type I and II magma experienced the substantial magmatic recharge-mixing event from the deeper source, where the injection of a hotter and less evolved magma results in partial dissolution of the preexisting crystal surfaces and crystallization of more mafic crystal layer (i.e., higher Ca/Mg/Fe) and vice versa (de Silva et al., 2008; Renjith, 2014). The fact that F2—P and F5—P layer has bimodal bulk-rock compositions (Fig. 7) may suggest both eruptions occurred just after the injection (i.e., magma mingling), without experiencing any magma hybridization. While the remaining layers (F1—P, F3—P, F4—P, Trayem, Jurangjero 1, Jurangjero 2, and F6—P) may have experienced magma hybridization prior to eruption, yielding the relatively homogeneous bulk-rock composition (Fig. 7). This magma recharge-hybridization is a common feature that triggers some of well-known sub-Plinian/Plinian eruptions, such as the 12 ka eruption of Popocatépetl (Malinche Pumice II stage), the <5 ka eruption of Agnano-Monte Spina, the 2000 cal. BP eruption of El Misti, the 550 cal. BP eruption of El Chichón, the 1875 CE eruption of Askja, and the 1471, 1779, and 1914 CE eruptions of Sakurajima (Mangler et al., 2020, Espinosa et al., 2021; Pelullo et al., 2022; Tepley et al., 2013; Macías et al., 2003, Andrews et al., 2008; Sigurdsson and Sparks, 1981; Araya et al., 2019). Moreover, this implies that such a complex architecture of the magma plumbing system at Merapi (i.e., consisting of numerous vertically-distributed and connected magmatic reservoirs between 700 and 100 MPa; Costa et al., 2013, Chadwick et al., 2013, van der Zwan et al., 2013, Widiyantoro et al., 2018) has been established at least since the Young Merapi stage.

5.2. The role of silica and temperature

Magmas decompress during eruption, resulting in vesiculation (mainly of H_2O) and crystallization, forming matrix-bubbles and microlites. Under the assumption of homogeneous nucleation, the correlation between MVND and MND should be theoretically positive (Toramaru, 2006; Toramaru et al., 2008). Here, we confirm that the positive correlation between MVND and MND is observed in this Young Merapi case (Fig. 11g), with both parameters having strong dependance on silica content (Fig. 11d, f).

It is known that higher SiO_2 magma tend to have low diffusivities and high surface tensions because of the high magma viscosity (Zhang and Behrens, 2000, Behrens et al., 2004, Toramaru, 2006, Takeuchi, 2011, Nishiwaki and Toramaru, 2019). Such conditions allow evolved magmas to experience a more extensive matrix-bubble nucleation (via second nucleation) during eruption, as well as inhibiting bubble expansion and coalescence during magma ascent (Toramaru, 2006) (Fig. 12). With those considerations, it is natural that the eruption of more silicic type II magma yielded pumice with higher MVNDs than pumice from type I magma (Fig. 11). Moreover, because the cooling of the magma would have resulted in crystallization and differentiation (see Section 6.1.), and colder magma facilitates larger degree of supercooling, microlite crystallization is expected to occur at higher and lower pressure condition for type II and type I magma, respectively (Fig. 12). This process allowed type II magma to experience deeper and more extensive microlite crystallization than type I, yielding a microlite-rich pumice for type II and microlite-poor pumice for type I. Because pyroxene and plagioclase were observed as two of the most abundant microlite phases (Fig. 6), and the crystallization of both minerals consumes calcium in the melt, the more extensive microlite crystallization plays a role for the more significant decrease of CaO_{glass}, such as those observed in F4—P and Trayem samples (Fig. 11i).

Finally, since MVND is a function of magma decompression rate (Toramaru, 2006), it is expected that type II magma experienced faster ascent rate than type I magma. To be quantitative, by assuming homogeneous nucleation with initial conditions of 5 wt% H_2O, 200 MPa initial saturation pressure (Costa et al., 2013, Innocenti et al., 2013; see Section 5.1.), and 0.07 N/m surface tension (typical surface tension for andesitic melts; Gardner et al., 2013), magma decompression rates vary from 5.3 to 12.4 MPa/s for type I and 5.5–19.3 MPa/s for type II, equivalent to that of the 2008 CE sub-Plinian eruption of Chaitén in Chile (12.1 ± 4.3 MPa/s; Alfano et al., 2012). This may be the reason why type II magma produced thicker deposits (Fig. 2) than type I magma; higher magma decompression rate yields higher eruption plume, yielding a larger dispersal area (Toramaru, 2006; Bonadonna and Costa, 2013). In addition, the fact that many plagioclase and pyroxene phenocrysts are fractured and coarsely sieved (both for type I and II pumice; Fig. 5b-d) also supports the idea of high magma decompression rates (Nelson and Montana, 1992; Viccaro et al., 2010; Renjith, 2014; van Zalinge et al., 2018). Nevertheless, some studies have shown that the MVND-decompression rate meter always yields a significantly higher ascent rate (up to two to three orders of magnitude difference) compared to the other methods such as the microlite textures, melt embayment, broken crystals, and amphibole breakdown rims (e.g., Shea, 2017; Cassidy et al., 2018). Thus, to be fair, we have to address that our estimation on the magma decompression rate values using MVND may be overestimated. Moreover, decompressing magma from the reservoir (200 MPa) to the surface at 5–19 MPa/s indicates a magma ascent velocity of 200–760 m/s; this suggest that the magma ascended from the reservoir towards the surface just within 11–40 s, which is extremely fast. This discrepancy occurs because: (1) the MVND may only record the final decompression stage, not the entire decompression path, and (2) the decompression rate can be non-linear, thus may accelerate as the magma ascends (Mastin and Ghiorso, 2000, Mastin, 2002, Nowak et al., 2011). Further examination is strongly needed to solve these problems and will be out of the scope of this paper.

5.3. The importance of preexisting lava dome for generating explosive sub-Plinian/Plinian eruptions: Insights from componentry

It is known that the presence of a lava dome can lead to gas accumulation (i.e., overpressure) in the conduit (Woods, 1995; Sparks, 1997; Sigurdsson, 2000). Consequently, when the overpressure exceeds the strength of the dome, an eruption occurs, causing a sudden decompression that facilitates substantial gas exsolution from magma. This is the reason why numerous mild (VEI 3–5) sub-Plinian/Plinian eruptions were preceded by dome formation (at least few years before the explosive event), such as the 2008 CE eruption of Chaiten (η and λ layer), 2010 CE eruption of Merapi, and 2014 CE eruption of Kelud (Alfano et al., 2011, 2012; Surono et al., 2012; Cronin et al., 2013; Jeffery et al., 2013; Maeno et al., 2019). As a result, this kind of eruptive style generally yields abundant pumice clasts with substantial amount of lithics (15–50% C_{lithic}) (e.g., Maeno et al., 2019, Müller et al., 2022) (Fig. 13). For comparison, another mild sub-Plinian/Plinian eruptions with no initial dome formation produces a characteristically lithic-poor deposits (<10% C_{lithic}, with a predominantly <5% C_{lithic}), such as the 60 ka Fontana Lapilli eruption, 640 CE Newberry eruption (the "Big Obsidian Flow"), 1886 CE Tarawera eruption, 1914–15 CE Sakurajima eruption ("Taisho"), 1986 CE Izu-Oshima eruption, and 2015 CE Calbuco eruption (Costantini et al., 2010; Trafton and Giachetti, 2022; Walker et al., 1984; Todde et al., 2017; Sumner, 1998; Castruccio et al., 2016) (Fig. 13). In addition, a Vulcanian eruption (mostly VEI <3) is characterized by the domination of lithics instead of juvenile clasts (up to ~90% C_{lithic}; e.g., Alfano et al., 2011, 2012, Maeno et al., 2023) (Fig. 13).

In this study, we found that all Young Merapi pumice fall deposits include substantial amount of volcanic lithics (11–50% C_{lithic}) (Fig. 13). Note that such lithic variations are not typical in dome-free sub-Plinian/Plinian and Vulcanian eruptions as mentioned above. Moreover, the fact that most lithics displayed fresh condition with abundant phenocryst contents (Fig. 4a) strongly suggest that these lithics were originated from the preexisting lava dome (i.e., lava domes in intermediate system were typically phenocryst-rich; e.g., Murase et al., 1985, Yokoyama,

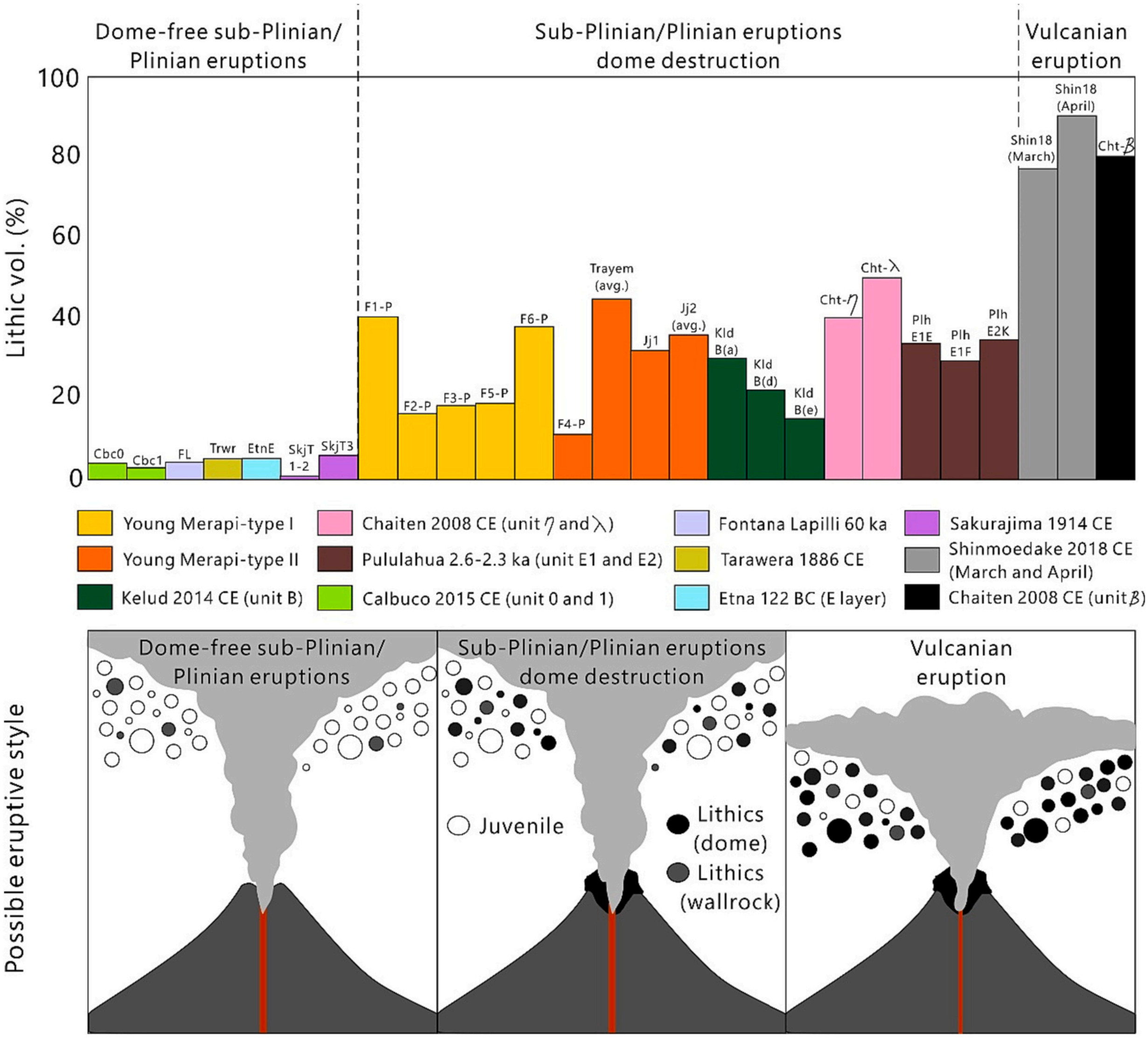

Fig. 13. Comparison on lithic contents among some famous VEI 3–5 eruptions worldwide. Sub-Plinian/Plinian eruptions without initial dome formation (dome-free) is characterized by the typically low abundance of lithics ($<10\%$ C_{lithic}). Sub-Plinian/Pliniana eruptions dome destruction are typically had substantial amount of lithics, varying from >10 to 50% C_{lithic}. While vulcanian eruptions are characterized by the domination lithics instead the juvenile (up to ∼90% C_{lithic}).

2005, Jeffery et al., 2013). Thus, we suggest that all pumice fall deposits during the Young Merapi phase always initiated by dome formation, similar to that of the Modern Merapi case (e.g., the 1872 and 2010 CE eruption; Gertisser et al., 2012, Surono et al., 2012, Cronin et al., 2013). This is significant because the explosive behavior (sub-Plinian/Plinian) at Merapi have been constant (at least) during the past ∼2 ka years. In addition, in the case of sub-Plinian/Plinian eruptions, it is clear that thicker deposits (i.e., more voluminous eruption) typically produces more abundant lithics than that the thinner ones (Fig. 4c). Thus, we suggest that a larger eruption intensity (i.e., more explosive eruption; higher MVND) yields more significant dome destruction and wall-rock erosion (Sable et al., 2006; Shea et al., 2012).

5.4. Comparison to the other basalt-basaltic andesite sub-Plinian/Plinian eruptions

Previously, mafic magmas (basalt–basaltic andesite bulk-rock compositions) were underestimated for their capability to produce explosive eruptions due to their low viscosities ($<10^4$ Pa s; Takeuchi, 2011). However, recent studies have revealed that such mafic magma compositions are capable to produce explosive eruptions with sub-Plinian or Plinian intensity (with VEIs ranging from 3 to 5), such as the 60 ka eruption of Fontana Lapilli, the 122 BCE eruption of Etna, the 1886 CE eruption of Tarawera, the 1986 CE eruption of Izu-Oshima, the 1990 CE and 2014 CE eruptions of Kelud, and the undated eruption of Kukusan (Costantini et al., 2010; Sable et al., 2006; Walker et al., 1984; Ikehata et al., 2010; Bourdier et al., 1997, Maeno et al., 2019; Mitsuoka et al., 2021). Merapi is not an exception, as most of its explosive products (i.e., pumice and/or scoria) are basalt and basaltic andesite (Gertisser et al., 2012; Costa et al., 2013).

The reason why Young Merapi is able to achieve sub-Plinian and/or Plinian intensity and attained the highest MVNDs value among all reported mafic explosive eruptions (e.g., Fontana Lapilli, Etna, Tarawera, Izu-Oshima, and Kukusan; Costantini et al., 2010; Sable et al., 2006; Walker et al., 1984; Ikehata et al., 2010; Mitsuoka et al., 2021) is because of its evolved glass compositions (Figs. 7e and 14), reaching andesite to dacite (see Section 5.2). However, it is important to note that the explosive eruptions of the Young Merapi were less voluminous (VEI 3–4) compared to the other famous sub-Plinian and/or Plinian eruptions (VEI 4–5) (Fig. 14). This might be related to pheno-crystallinity in the pre-eruptive magma chamber. In particular, the product of VEI 3–4 eruptions of the Young Merapi are typically phenocryst-rich ($>0.4\ \overset{\circ}{\varphi}_{PC}$),

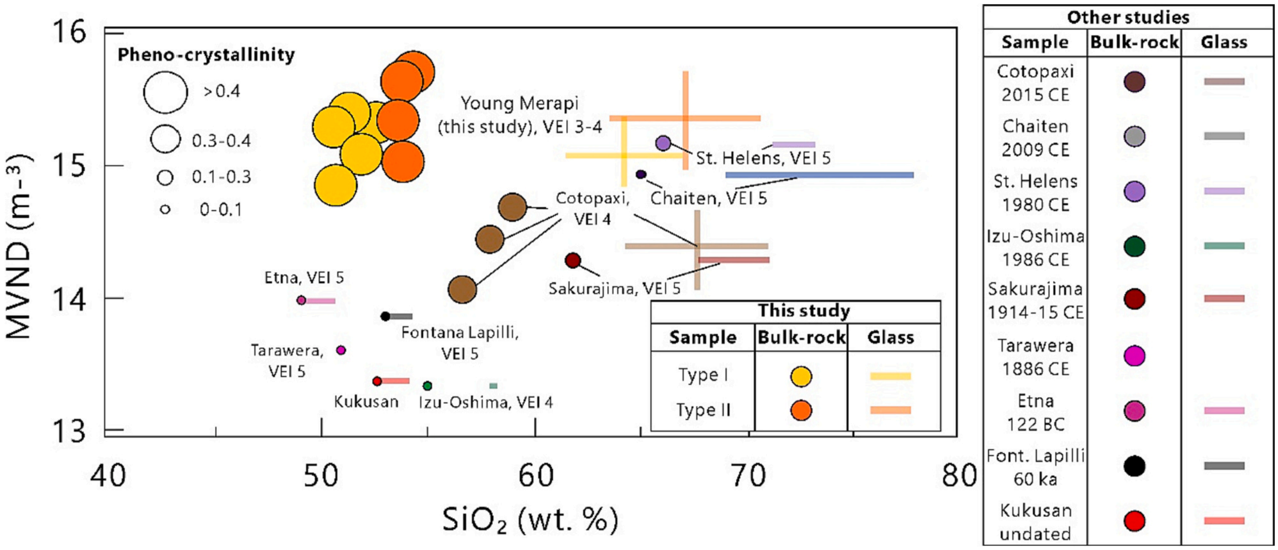

Fig. 14. Comparison of MVND and SiO_2 plot between the Young Merapi pumices (this study, shown by yellow and orange circles) with juveniles from the other sub-Plinian/Plinian eruptions. Note that each circle size denotes different pheno-crystallinity value. Larger eruptions (VEI 5) tend to be associated with less crystalline magma (30% pheno-crystallinity), while smaller eruptions (VEI 3–4) include more phenocrysts (up to >40%). (For interpretation of the references to colour in this figure legend, the reader is referred to the web version of this article.)

while the product of VEI 5 eruptions is typically having a significantly lower pheno-crystallinity ($<0.3\ \mathring{\varphi}_{PC}$, with a predominantly $<0.1\ \mathring{\varphi}_{PC}$) (Fig. 14). This may suggest that a highly crystalline magma tends to be less-eruptible than the less crystalline ones, and consequently, terminates the eruption quickly. As time goes by, it is very likely that phenocrysts in both magma types will undergo crystal settling process, causing a stratification in the magma chamber (i.e., the upper portion is more evolved and phenocryst-poor, while the lower portion tend to be less evolved and phenocryst-rich; e.g., Ginibre et al., 2004, Suhendro et al., 2021). If this scenario occurs, the portion of eruptible magma increases, thus may allow a more voluminous eruption (larger VEI) in future; therefore, we suggest that geophysical modelling of the modern Merapi magmatic system will be crucial for eruption forecasting and hazard mitigation.

6. Conclusion

The results of petrography, bulk-rock, glass, and feldspar compositions suggest that (at least) two different magmatic bodies are sourcing the explosive eruptions during the Young Merapi stage. Type I is slightly more mafic than type II, as suggested by the abundance of pyroxene, lower bulk-rock and glass silica contents, and more calcic feldspar microlite compositions. These conditions strongly suggest that type I magma is hotter than type II. The prevalence of disequilibrium textures in plagioclase and pyroxene phenocrysts (i.e., finely sieved and reversely and oscillatory zoned) strongly suggests that the complex architecture of the magma plumbing system at Merapi (i.e., consisting of numerous vertically-distributed and connected magmatic reservoirs between 700 and 100 MPa) has been established at least since the Young Merapi stage. Furthermore, type I pumice typically has lower MVND and MND values compared to type II, suggesting that type I magma experienced less intense matrix-bubble nucleation and microlite crystallization due to lower SiO_2 and higher temperature conditions. This implies that the eruption of type I magma was less explosive than type II magma. Noteworthy, the fact that all deposits include a substantial amount of fresh- and phenocryst-rich volcanic lithics (11–50% C_{lithic}) suggests that the explosive eruptions of the Young Merapi were always initiated by dome formation, similar to that of the Modern Merapi case (e.g., the 1872 and 2010 CE eruption). Finally, we also pointed out that the relatively small volume (VEI 3–4) of the Young Merapi eruptions might be caused by the mushy condition of the magma reservoirs ($>0.4\ \mathring{\varphi}_{PC}$); namely, highly crystalline magma tends to be less-eruptible than the less crystalline ones, thus terminating the eruption quickly.

Credit author statement

I.S. conceptualized the research, conducted fieldwork, undertook grain size distribution (GSD), componentry and textural analyses, data curation, interpreted the data, make all visualizations, and wrote the initial manuscript. **G.N.R.B.N.** conducted petrography, SEM, FE-EPMA, and some textural analyses. **A.G.** conducted bulk-rock XRF and some textural analysis. **S.A.S., M.L.A.M., M.F.Q.,** and **F.S.** joined the fieldwork, undertook GSD, componentry, and some textural analyses. **R.M.P.P.G., J.J., S.MC.** and **D.N.A.** undertook componentry and some textural analyses. **All authors** contributed to refining the manuscript.

I.S. = Indranova Suhendro.
G.N.R.B.N. = Gabriela Nogo Retnaningtyas Bunga Naen.
A.G. = Andriansyah Gurusinga.
S.A.S. = Sistien Adhaena Sari.
M.L.A.M. = Mradipta Lintang Alifcanta Moktikanana.
R.M.P.P.G. = Rachmi Mustika Pertiwi Putri Gunawan.
J.J. = Jesslyn Jane.
M.F.Q. = Muhammad Fatih Qodri.
F.S. = Faraz Sya'bana.
S.M.C. = Sherinna Mega Cahyani.
D.N.A. = Dini Nuari Ardian.

Declaration of Competing Interest

The authors declare that they have no known competing financial interests or personal relationships that could have appeared to influence the work reported in this paper.

Data availability

Data will be made available on request.

Acknowledgement

We are grateful to Prof. A. Toramaru and Prof. T. Ohba for their permission of using laboratory facilities at the Department of Earth and Planetary Sciences, Kyushu University and Department of Earth Resource Science, Akita University, respectively. We thank B.J. Andrews, L. Gurioli, and Claudia D'Oriano for their critical reviews and constructive comments, and Ed Llewelin for editorial handling. We also thank K. Shimada for his technical support during the FE-EPMA analysis, and Catherine H. Mulyadi for sample distribution (from Indonesia to Japan).

References

Adams, N.K., Houghton, B.F., Hildreth, W., 2006. Abrupt transitions during sustained explosive eruptions: examples from the 1912 eruption of Novarupta, Alaska. Bull. Volcanol. 69, 189–206. https://doi.org/10.1007/s00445-006-0067-4.

Alfano, F., Bonadonna, C., Volentik, A.C.M., Connor, C.B., Watt, S.F.L., Pyle, D.M., Connor, L.J., 2011. Tephra stratigraphy and eruptive volume of the May, 2008, Chaitén eruption, Chile. Bull. Volcanol. 73, 613–630. https://doi.org/10.1007/s00445-010-0428-x.

Alfano, F., Bonadonna, C., Gurioli, L., 2012. Insights into eruption dynamics from textural analysis: the case of the May, 2008, Chaitén eruption. Bull. Volcanol. 74, 2095–2108. https://doi.org/10.1007/s00445-012-0648-3.

Andreastuti, S., Alloway, B.V., Smith, I.E.M., 2000. A detailed tephrostratigraphic framework at Merapi Volcano, Central Java, Indonesia: implications for eruption predictions and hazard assesment. J. Volcanol. Geotherm. Res. 100, 51–67. https://doi.org/10.1016/S0377-0273(00)00133-5.

Andrews, B.J., Gardner, J.E., Housh, T.B., 2008. Repeated recharge, assimilation, and hybridization in magmas erupted from El Chichón as recorded by plagioclase and amphibole phenocrysts. J. Volcanol. Geotherm. Res. 175, 415–426. https://doi.org/10.1016/j.jvolgeores.2008.02.017.

Araya, N., Nakamura, M., Yasuda, A., Okumura, S., Sato, T., Iguchi, M., Miki, D., Geshi, N., 2019. Shallow magma pre-charge during repeated Plinian eruptions at Sakurajima volcano. Sci. Rep. 9, 1979. https://doi.org/10.1038/s41598-019-38494-x.

Behrens, H., Zhang, Y., Xu, Z., 2004. H_2O diffusion in dacitic and andesitic melts. Geochemica et Cosmochimica Acta 68, 5139–5150. https://doi.org/10.1016/j.gca.2004.07.008.

Bernard, O., de Maisonneuve, C.B., 2020. Controls on eruption styles at Rabaul, Papua New Guinea – insights from microlites, porosity and permeability measurements. J. Volcanol. Geotherm. Res. 406, 107068. https://doi.org/10.1016/j.jvolgeores.2020.107068.

Berthommier, P.C., 1990. Etude volcanologique du Merapi (Centre-Java) Téphrostrartigraphie et chronologie–mécanismes éruptifs. Unpublished thesis. University of Blaise Pascal, Clermont Ferrand, 115 pp., annexes.

Bonadonna, C., Costa, A., 2013. Plume height, volume, and classification of explosive volcanic eruptions based on the Weibull function. Bull. Volcanol. 75, 742. https://doi.org/10.1007/s00445-013-0742-1.

Bourdier, J.L., Pratomo, I., Thouret, J.C., Boudon, G., Vincent, P.M., 1997. Observations, stratigraphy and eruptive processes of the 1990 eruption of Kelut volcano, Indonesia. J. Volcanol. Geotherm. Res. 79, 181–203. https://doi.org/10.1016/S0377-0273(97)00031-0.

Bunga Naen, G.N.R., Toramaru, A., Juhri, S., Yonezu, K., Wibowo, H.E., Gunawan, R.M.P.P., Disando, T., 2023. Distinct pumice populations in the 74 ka Youngest Toba Tuff: evidence for eruptions from multiple magma chambers. J. Volcanol. Geotherm. Res. 437, 107804. https://doi.org/10.1016/j.jvolgeores.2023.107804.

Camus, G., Gourgaud, A., Mossand-Berthommierr, P., Vincent, P.M., 2000. Merapi (Central Java, Indonesia): an outline of the structural and magmatological evolution, with a special emphasis to the major pyroclastic events. J. Volcanol. Geotherm. Res. 100, 139–163. https://doi.org/10.1016/S0377-0273(00)00135-9.

Cassidy, M., Manga, M., Cashman, K.V., Bachmann, O., 2018. Controls on explosive-effusive volcanic eruption styles. Nature Communications 9, 2839. https://doi.org/10.1038/s41467-018-05293-3.

Castruccio, A., Clavero, J., Segura, A., Samaniego, P., Roche, O., Le Pennec, J.L., Droguett, B., 2016. Eruptive parameters and dynamics of the April 2015 sub-Plinian eruptions of Calbuco volcano (southern Chile). Bulletin of Volcanology 78, 62. https://doi.org/10.1007/s00445-016-1058-8.

Chadwick, J.P., Troll, V.R., Waight, T.E., van der Zwan, F.M., Schwarzkopf, L.M., 2013. Petrology and geochemistry of igneous inclusions in recent Merapi deposits: a window into the sub-volcanic plumbing system. Contrib. Mineral. Petrol. 165, 259–282. https://doi.org/10.1007/s00410-012-0808-7.

Cherniak, D.J., Watson, E.B., 1994. A study of strontium diffusion in plagioclase using Rutherford backscattering spectroscopy. Geochemica et Cosmochimica Acta 58 (23), 5179–5190. https://doi.org/10.1016/0016-7037(94)90303-4.

Cichy, S.B., Botcharnikov, R.E., Holtz, F., Behrens, H., 2011. Vesiculation and microlite crystallization induced by decompression: a case study of the 1991-1995 Mt Unzen eruption (Japan). J. Petrol. 32 (7–8), 1469–1492. https://doi.org/10.1093/petrology/egq072.

Costa, F., Andreastuti, S., Bouvet de Maisonneuve, C., Pallister, J.S., 2013. Petrological insights into the storage conditions, and magmatic processes that yielded the centennial 2010 Merapi explosive eruption. J. Volcanol. Geotherm. Res. 261, 209–235. https://doi.org/10.1016/j.jvolgeores.2012.12.025.

Costantini, L., Houghton, B.F., Bonadonna, C., 2010. Constraints on eruption dynamics of basaltic explosive activity dedrived from chemical and microtextural study: the example of the Fontana Lapilli Plinian eruption, Nicaragua. J. Volcanol. Geotherm. Res. 189, 207–224. https://doi.org/10.1016/j.jvolgeores.2009.11.008.

Couch, S., Harford, C.L., Sparks, R.S.J., Carrol, M.R., 2003. Experimental constraints on the conditions of formation of highly calcic plagioclase microlites at the Soufrière Hills volcano. Montserrat. J. Petrol. 44, 1455–1475. https://doi.org/10.1093/petrology/44.8.1455.

Cronin, S.J., Lube, G., Dayudi, D.S., Sumarti, S., Subrandiyo, S., Surono, 2013. Insights into the October-November 2010 Gunung Merapi eruption (Central Java, Indonesia) from the stratigraphy, volume and characteristics of its pyroclastic deposits. J. Volcanol. Geotherm. Res. 261, 244–259. https://doi.org/10.1016/j.jvolgeores.2013.01.005.

Darmawan, H., Troll, V.R., Walter, T.R., Deegan, F.M., Geiger, H., Heap, M.J., Seraphine, N., Harris, C., Humaida, H., Müller, D., 2022. Hidden mechanical weaknesses within lava domes provided by buried high-porosity hydrothermal alteration zones. Sci. Rep. 12, 3202. https://doi.org/10.1038/s41598-022-06765-9.

de Bélizal, E., Lavigne, F., Hadmoko, D.S., Degeai, J.P., Dipayana, G.A., Mutaqin, B.W., Marfai, M.A., Coquet, M., Le Mauff, B., Robin, A.K., Vidal, C., Cholik, N., Aisyah, N., 2013. Rain-triggered lahars following the 2010 eruption of Merapi volcano, Indonesia: A major risk. J. Volcanol. Geotherm. Res. 261, 330–347.

de Silva, S., Salas, G., Schubring, S., 2008. Triggering explosive eruptions–the case for silicic magma recharge at Huaynaputina, southern Peru. Geology 36 (5), 387–390. https://doi.org/10.1016/j.jvolgeores.2013.01.010.

Edmonds, M., Woods, A.W., 2018. Exsolved volatiles in magma reservoirs. J. Volcanol. Geotherm. Res. 368, 13–30. https://doi.org/10.1016/j.jvolgeores.2018.10.018.

Espinosa, V.D., Arce, J.L., Castro-Govea, R., 2021. Pre-eruptive conditions and reheating of dacitic magma (Malinche Pumice II Plinian eruption) at La Malinche volcano, Central Mexico. J. Volcanol. Geotherm. Res. 419, 107368. https://doi.org/10.1016/j.jvolgeores.2021.107368.

Forni, F., Bachmann, O., Mollo, S., De Astis, G., Gelman, S.E., Ellis, B.S., 2016. The origin of a zoned ignimbrite: Inisghts into the Campanian Ignimbrite magma chamber (Campi Flegrei, Italy). Earth Planet. Sci. Lett. 449, 259–271. https://doi.org/10.1016/j.epsl.2016.06.003.

Gardner, J.E., Ketcham, R.A., Moore, G., 2013. Surface tension of hydrous silicate melts: Constraints on the impact of melt composition. J. Volcanol. Geotherm. Res. 267, 68–74. https://doi.org/10.1016/j.jvolgeores.2013.09.007.

Gertisser, R., Keller, J., 2003. Trace element and Sr, Nd, Pb and O isotope variations in medium-K and high-K volcanic rocks from Merapi Volcano, Central Java, Indonesia: evidence for the involvement of subducted sediments in Sunda Arc magma genesis. Journal of Petrology 44 (3), 457–489. https://doi.org/10.1111/j.1365-2451.2011.00786.x.

Gertisser, R., Charbonnier, S.J., Troll, V.R., Keller, J., Preece, K., Chadwick, J.P., Barclay, J., Herd, R.A., 2011. Merapi (Java, Indonesia): anatomy of a killer volcano. The Geologists' Association & The Geological Society of London, Geology Today 27 (2), 57–62.

Gertisser, R., Charbonnier, S.J., Keller, J., Quidelleur, X., 2012. The geological evolution of Merapi volcano, Central Java, Indonesia. Bull. Volcanol. 74, 1213–1233. https://doi.org/10.1007/s00445-012-0591-3.

Gertisser, R., Troll, V.R., Walter, T.R., Nandaka, I.G.M.A., Ratdomopurbo, A., 2023. Merapi Volcano: Geology, Eruptive Activity, and Monitoring of a High-Risk Volcano. Springer. https://doi.org/10.1007/978-3-031-15040-1.

Ginibre, C., Wörner, G., Krornz, A., 2004. Structure and dynamics of the Laacher See magma chamber (Eifel, Germany) from major and trace element zoning in sanidine: a cathodoluminescence and electron microprobe study. J. Petrol. 45 (11), 2197–2223. https://doi.org/10.1093/petrology/egh053.

Gurioli, L., Houghton, B.F., Cashman, K.V., Cioni, R., 2005. Complex changes in eruption dynamics during the 79 AD eruption of Vesuvius. Bull. Volcanol. 67, 144–159. https://doi.org/10.1007/s00445-004-0368-4.

Hadmoko, D.S., de Belizal, E., Mutaqin, B.W., Dipayana, G.A., Marfai, M.A., Lavigne, F., Sartohadi, J., Worosuprojo, S., Starheim, C.C.A., Gomez, C., 2018. Post-eruptive lahars at Kali Putih following the 2010 eruption of Merapi volcano, Indonesia: occurrences and impacts. Nat. Hazards 94, 419–444. https://doi.org/10.1007/s11069-018-3396-7.

Hammer, J.E., Cashman, K.V., Hoblitt, R.P., Newman, S., 1999. Degassing and microlite crystallization during pre-climatic events of the 1991 eruption of Mt. Pinatubo, Philippines. Bull. Volcanol. 60, 355–380. https://doi.org/10.1007/s004450050238.

Handley, H.K., Macpherson, C.G., Davidson, J.P., Berlo, K., Lowry, D., 2007. Constraining Fluid and Sediment Contributions to Subduction-Related Magmatism in Indonesia: Ijen Volcanic complex. J. Petrol. 48 (6), 1155–1183. https://doi.org/10.1093/petrology/egm013.

Higgins, M.D., 2002. Quantitative Textural Measurements in Igneous and Metamorphic Petrology. Cambridge University Press.

Humphreys, M.C.S., Christoper, T., Hards, V., 2009. Microlite transfer by disaggregation of mafic inclusions following magma mixing at Sourfrière Hills volcano, Montserrat. Contrib. Mineral. Petrol. 157, 609–624. https://doi.org/10.1007/s00410-008-0356-3.

Ikehata, K., Yasuda, A., Notsu, K., 2010. The geochemistry of volatile species in melt inclusions and sulfide minerals from Izu-Oshima volcano, Japan. Mineral. Petrol. 99, 143–152. https://doi.org/10.1007/s00710-009-0086-x.

Innocenti, S., Andreastuti, S., Furman, T., del Marmol, M.A., Voight, B., 2013. The pre-eruption conditions for explosive eruptions at Merapi volcano as revealed by crystal texture and mineralogy. J. Volcanol. Geotherm. Res. 261, 69–86. https://doi.org/10.1016/j.jvolgeores.2012.12.028.

Jeffery, A.J., Gertisser, R., Troll, V.R., Jolis, E.M., Dahren, B., Harris, C., Tindle, A.G., Preece, K., O'Driscoll, B., Humaida, H., Chadwick, J.P., 2013. The pre-eruptive magma plumbing system of the 2007-2008 dome-forming eruption of Kelut volcano, East Java, Indonesia. Contrib. Mineral. Petrol. 166, 275–308. https://doi.org/10.1007/s00410-013-0875-4.

Kaneko, K., Kamata, H., Koyaguchi, T., Yoshikawa, M., Furukawa, K., 2007. Repeated large-scale eruptions from a single compositionally stratified magma chamber: an example from Aso volcano, Southwest Japan. J. Volcanol. Geotherm. Res. 167, 160–180. https://doi.org/10.1016/j.jvolgeores.2007.05.002.

Kelfoun, K., Gueugneau, V., 2022. A Unifying Model for Pyroclastic Surge Genesis and Pyroclastic Flow Fluidization. Geophys. Res. Lett. 49, 5. https://doi.org/10.1029/2021GL096517.

Klug, C., Cashman, K.V., 1994. Vesiculation of May 18, 1980, Mount St. Helens magma. Geology 22, 468–472. https://doi.org/10.1130/0091-7613(1994)022<0468:VOMMSH>2.3.CO;2.

Klug, C., Cashman, K.V., 1996. Permeability development in vesiculating magmas: implications for fragmentation. Bull. Volcanol. 58, 87–100. https://doi.org/10.1007/s004450050128.

Klug, C., Cashman, K.V., Bacon, C.R., 2002. Structure and physical characteristics of pumice from the climatic eruption of Mount Mazama (Crater Lake), Oregon. Bull. Volcanol. 64, 486–501. https://doi.org/10.1007/s00445-002-0230-5.

Lavigne, F., Thouret, J.C., Voight, B., Suwa, H., Sumaryono, A., 2000. Lahars at Merapi volcano, Central Java: an overview. J. Volcanol. Geotherm. Res. 100, 423–456. https://doi.org/10.1016/S0377-0273(00)00150-5.

Macías, J.L., Arce, J.L., Mora, J.C., Espíndola, J.M., Saucedo, R., 2003. A 550-year-old eruption at El Chichón Volcano, Chiapas, Mexico: Explosive volcanism linked to reheating of the magma reservoir. J. Geophys. Res. 108 (B12), 2569. https://doi.org/10.1029/2003JB002551.

Maeno, F., Nakada, S., Yoshimoto, M., Shimano, T., Hokanishi, N., Zaennudin, A., Iguchi, M., 2019. A sequence of a plinian eruption preceded by dome destrurction at Kelud volcano, Indonesia, on February 13, 2014, revealed from tephra fallout and pyroclastic density current deposits. J. Volcanol. Geotherm. Res. 382, 24–41. https://doi.org/10.1016/j.jvolgeores.2017.03.002.

Maeno, F., Shohata, S., Suzuki, Y., Hokanishi, N., Yasuda, A., Ikenaga, Y., Kaneko, T., Nakada, S., 2023. Eruption style transition during the 2017-2018 eruptive activity at the Shinmoedake volcano, Kirishima, Japan: surface phenomena and eruptive products. Earth Planets Space 75, 76. https://doi.org/10.1186/s40623-023-01834-3.

Mangler, M.F., Petrone, C.M., Hill, S., Delgado-Granados, H., Prytulak, J., 2020. A pyroxenic view on magma hybridization and crystallization at Popocatépetl volcano, Mexico. Front. Earth Sci. 8, 362. https://doi.org/10.3389/feart.2020.00362.

Marshall, A.A., Band, B.D., Martinez, V., Bowers, J.M., Walker, M., Wanless, V.D., Andrews, B.J., Manga, M., Valdivia, P., Giordano, G., 2022. The mafic Curacautin ignimbrite of Llaima volcano, Chile. J. Volcanol. Geotherm. Res. 421, 107418. https://doi.org/10.1016/j.jvolgeores.2021.107418.

Mastin, L.G., 2002. Insights into volcanic conduit flow from an open-source numerical model. Geochem. Geophys. Geosyst. 3, 7. https://doi.org/10.1029/2001GC000192.

Mastin, L.G., Ghiorso, M.S., 2000. A numerical program for steady-state flow of magma-gas mixturers through vertical eruption conduits. USGS Open-File Report 00–209.

McBirney, A.R., 2007. Igneous Petrology, third edition. Jones and Bartlett, Burlington.

Mitsuoka, T., Toramaru, A., Harijoko, A., Wibowo, H.E., 2021. Eruption Types and Conduit Dynamics of Kukusan and Genteng Volcanoes of the Ijen Volcanic complex, Indonesia. Kyushu University Institutional Repository: Series D, Earth and Planetary Sciences 35 (1), 1–17. https://doi.org/10.5109/4371995.

Morgan, D.J., Jerram, D.A., 2006. On estimating crystal shape for crystal size distribution analysis. J. Volcanol. Geotherm. Res. 154 https://doi.org/10.1016/j.jvolgeores.2005.09.016.

Müller, A.V., Cashman, K.V., Mitchell, S.J., Vasconez, F.J., 2022. The 2.6-2.3 ka explosive eruptive period of the Pululahua dome complex, Ecuador: insights from pyroclast analysis. Bull. Volcanol. 84, 81. https://doi.org/10.1007/s00445-022-01590-4.

Murase, T., McBirney, A.R., Melson, W.G., 1985. Viscosity of the dome of Mount St. Helens. Journal of Volcanology and Geothermal Research 24, 193–204. https://doi.org/10.1016/0377-0273(85)90033-2.

Namur, O., Montalbano, S., Bolle, O., Auwera, J.V., 2020. Petrology of the April 2015 eruption of Calbuco volcano, Southern Chile. J. Petrol. 61, 8. https://doi.org/10.1093/petrology/egaa084.

Nelson, S.T., Montana, A., 1992. Sieve-textured plagioclase in volcanic rocks produced by rapid decompression. Am. Mineral. 77 (11–12), 1242–1249.

Newhall, C.G., Bronto, S., Alloway, B., Banks, N.G., Bahar, I., del Marmol, M.A., Hadisantono, R.D., Holcomb, R.T., McGeehin, J., Miksic, J.N., Rubin, M., Sayudi, S. D., Sukhyar, R., Andreastuti, S., Tilling, R.I., Torley, R., Trimble, D., Wirakusumah, A.D., 2000. 10,000 years of explosive eruptions of Merapi Volcano, Central Java: archaeological and modern implications. J. Volcanol. Geotherm. Res. 100, 9–50. https://doi.org/10.1016/S0377-0273(00)00132-3.

Nishiwaki, M., Toramaru, A., 2019. Inclusions of Viscosity into classical homogeneous nucleation theory for water bubbles in silicate melts: reexamination of bubble number density in ascending magmas. J. Geophys. Res. Solid Earth 1214, 8250–8266. https://doi.org/10.1029/2019JB017796.

Nowak, M., Cichy, S.B., Botcharnikov, R.E., Walker, N., Hurkuck, W., 2011. A new type of high-pressure low-flow metering valve for continuous decompression: first experimental results on degassing of rhyodacitic melts. Am. Mineral. 96, 8–9. https://doi.org/10.2138/am.2011.3786.

Pallister, J.S., Hoblitt, R.P., Meeker, G.P., Knight, R.J., Siems, D.F., 1996. Magma mixing at Mount Pinatubo; petrographic and chemical evidence from the 1991 deposits. In: Newhall, C.G., Punongbayan, R.S. (Eds.), Fire and Mud. Eruption and lahars of Mount Pinatubo, Philippines, pp. 687–731.

Pelullo, C., Chakraborty, S., Cambeses, A., Dohmen, R., Arienzo, I., D'Antonio, M., Pappalardo, L., Petrosino, P., 2022. Insights into the temporal evolution of magma plumbing systems from compositional zoning in clinopyroxene crystals from the Agnano-Monte Spina Plinian eruption (Campi Flegrei, Italy). Geochim. Cosmochim. Acta 328, 185–206. https://doi.org/10.1016/j.gca.2022.04.007.

Phuong, N.K., Harijoko, A., Itoi, R., Unoki, Y., 2012. Water geochemistry and soil gas survey at Ungaran geothermal field, Central Java, Indonesia. J. Volcanol. Geotherm. Res. 229-2330, 23–33. https://doi.org/10.1016/j.jvolgeores.2012.04.004.

Polacci, M., Papale, P., Rosi, M., 2001. Textural heterogeneities in pumices from the climatic eruption of Mount Pinatubo, 15 June 1991, and implications for magma ascent dynamics. Bull. Volcanol. 63, 83–97. https://doi.org/10.1007/s004450000123.

Preece, K., Gertisser, R., Barclay, J., Charbonnier, S.J., Komorowski, J.C., Herd, R.A., 2016. Transitions between explosive and effusive phases during the cataclysmic 2010 eruption of Merapi volcano, Java, Indonesia. Bull. Volcanol. 78, 54. https://doi.org/10.1007/s00445-016-1046-z.

Renjith, M.L., 2014. Micro-textures in plagioclase from 1994-1995 eruption, Barren Island Volcano: evidence of dynamic magma plumbing system in the Andaman subduction zone. Geosci. Front. 5, 113–126. https://doi.org/10.1016/j.gsf.2013.03.006.

Ridolfi, F., Renzulli, A., 2012. Calcic amphiboles in calc-alkaline and alkaline magmas: thermobarometric and chemometric empirical equations valid up to 1,130°C and 2.2 GPa. Contrib. Mineral. Petrol. 163, 877–895. https://doi.org/10.1007/s00410-011-0704-6.

Ruth, D.C.S., Costa, F., 2021. A petrological and conceptual model of Mayon volcano (Philippines) as an example of an open-vent volcano. Bull. Volcanol. 83, 62. https://doi.org/10.1007/s00445-021-01486-9.

Sable, J.E., Houghton, B.F., Del Carlo, P., Coltelli, M., 2006. Changing conditions of magma ascent and fragmentation during the Etna 122 BC basaltic Plinian eruption: evidence from clast microtextures. J. Volcanol. Geotherm. Res. 158, 333–354. https://doi.org/10.1016/j.jvolgeores.2006.07.006.

Salisbury, M.J., Bohrson, W.A., Clynne, M.A., Ramos, F.C., Hoskin, P., 2008. Multiple plagioclase crystal populations identified by crystal size distribution and *in situ* chemical data: Implications for timescales of magma chamber processes associated with the 1915 eruption of Lassen Peak, CA. J. Petrol. 49, 1755–1780. https://doi.org/10.1093/petrology/egn045.

Shea, T., 2017. Bubble nucleation in magmas: A dominantly heterogeneous process? J. Volcanol. Geotherm. Res. 343, 155–170. https://doi.org/10.1016/j.jvolgeores.2017.06.025.

Shea, T., Larsen, J.F., Gurioli, L., Hammer, J.E., Houghton, B.F., Cioni, R., 2009. Leucite crystals: surviving witnesses of magmatic processes preceding the 79 AD eruption at Vesuvius, Italy. Earth Planet. Sci. Lett. 281, 88–98. https://doi.org/10.1016/j.epsl.2009.02.014.

Shea, T., Gurioli, L., Houghton, B.F., 2012. Transitions between fall phases and pyroclastic density currents during the AD 79 eruption at Vesuvius: building a transient conduit model from the textural and volatile record. Bull. Volcanol. 74, 2363–2381. https://doi.org/10.1007/s00445-012-0668-z.

Shimomura, M., Putra, R., Rukmini, N.A., Sulistiyani, 2019. Numerical simulation of Mt. Merapi pyroclastic flow in 2010. Journal of Disaster Research 14 (1), 105–115. https://doi.org/10.20965/jdr.2019.p0105.

Sigurdsson, H., 2000. Encyclopedia of Volcanoes. Academic Press.

Sigurdsson, H., Sparks, R.S.J., 1981. Petrology of rhyolitic and mixed magma ejecta from the 1875 eruption of Askja, Iceland. J. Petrol. 22, 41–84. https://doi.org/10.1093/petrology/22.1.41.

Simmons, J.M., Carey, R.J., Cas, R.A.F., Druitt, T.H., 2017. High magma decompression rates at the peak of a violent caldera-forming eruption (lower Pumice 1 eruption, Santorini, Greece). Bull. Volcanol. 79, 42. https://doi.org/10.1007/s00445-017-1120-1.

Solikhin, A., Thouret, J.C., Liew, S.C., Gupta, A., Sayudi, D.S., Oehler, J.F., Kassouk, Z., 2015. High-spatial-rersolution imagery helps map deposits of the large (VEI 4) 2010 Merapi volcano eruption and their impact. Bull. Volcanol. 77, 20. https://doi.org/10.1007/s00445-015-0908-0.

Sparks, R.S.J., 1997. Causes and consequences of pressurization of lava dome eruptions. Earth Planet. Sci. Lett. 150 (3–4), 177–189. https://doi.org/10.1016/S0012-821X(97)00109-X.

Streck, M.J., Wacaster, S., 2006. Plagioclase and pyroxene hosted melt inclusions in basaltic andesites of the current eruption of Arenal volcano, Costa Rica. J. Volcanol. Geotherm. Res. 1517, 236–253. https://doi.org/10.1016/j.jvolgeores.2006.03.040.

Suhendro, I., Toramaru, A., Miyamoto, T., Miyabuchi, Y., Yamamoto, T., 2021. Magma chamber stratification of the 1815 Tambora caldera-forming eruption. Bull. Volcanol. 83, 63. https://doi.org/10.1007/s00445-021-01484-x.

Suhendro, I., Toramaru, A., Harijoko, A., Wibowo, H.E., 2022. The origins of transparent and non-transparent white pumice: A case study of the 52 ka Maninjau caldera-forming eruption, West Sumatra, Indonesia. Journal of Volcanology and Geothermal Research 107643. https://doi.org/10.1016/j.jvolgeores.2022.107643.

Sumner, J.M., 1998. Formation of classtogenic lava flows during fissure eruption and scoria cone collapse: the 1986 eruption of Izu-Oshima volcano, eastern Japan. Bull. Volcanol. 60, 195–212. https://doi.org/10.1007/s004450050227.

Surono, Jousset, P., Pallister, J., Boichu, M., Buongiorno, M.F., Budissantoso, A., Costa, F., Andreastuti, S., Prata, F., Schneider, D., Clarisse, K., Humaida, H., Sumarti, S., Bignami, C., Griswold, J., Carn, S., Oppenheimer, C., Lavigne, F., 2012. The 2010 explosive eruption of Java's Merapi volcano-A '100 year' event. J. Volcanol. Geotherm. Res. 241-242, 121–135. https://doi.org/10.1016/j.jvolgeores.2012.06.018.

Takeuchi, S., 2011. Preeruptive magma viscosity: An important measure of magma eruptibility. J. Geophys. Res. Solid Earth 116. https://doi.org/10.1029/2011JB008243.

Tepley, F.J., da Silva, S., Salas, G., 2013. Magma dynamics and petrological evolution leading to the VEI 5 2000 BP eruption of El Misti Volcano, Southern Peru. J. Petrol. 54, 2033–2065. https://doi.org/10.1093/petrology/egt040.

Todde, A., Cioni, R., Pistolesi, M., Geshi, N., Bonadonna, C., 2017. The 1914 Taisho eruption of Sakurajima volcano: stratigraphy and dynamics of the largest explosive event in Japan during the twentieth century. Bull. Volcanol. 79, 72. https://doi.org/10.1007/s00445-017-1154-4.

Toramaru, A., 2006. BND (bubble number density) decompression rate meter for explosive volcanic eruptions. J. Volcanol. Geotherm. Res. 154, 303–316. https://doi.org/10.1016/j.jvolgeores.2006.03.027.

Toramaru, A., 2014. On the second nucleation of bubbles in magmas under sudden decompression. Earth Planet. Sci. Lett. 404, 190–199. https://doi.org/10.1016/j.epsl.2014.07.035.

Toramaru, A., 2019. Vesiculation and Crystallization of Magma: Fundamentals of volcanic eruption Process. University of Tokyo Press, p. 480 (in Japanese).

Toramaru, A., Noguchi, S., Oyoshihara, S., Tsune, A., 2008. MND (microlite number density) water exsolution rate meter. J. Volcanol. Geotherm. Res. 175, 156–167. https://doi.org/10.1016/j.jvolgeores.2008.03.035.

Trafton, K.R., Giachetti, T., 2022. The pivotal role of Vulcanian activity in ending the explosive phase of rhyolitic eruptions: the case of the big Obsidian Flow eruption (Newberry Volcano, USA). Bull. Volcanol. 84, 104. https://doi.org/10.1007/s00445-022-01610-3.

Turner, S., Foden, J., George, R., Evans, P., Varne, R., Elburg, M., Jenner, G., 2003. Rates and processes of potassic magma evolution beneath Sanggeang Api volcano, East Sunda arc, Indonesia. Journal of Petrology 44 (3), 491–515. https://doi.org/10.1093/petrology/44.3.491.

Van Bemmelen, 1949. The geology of Indonesia, vol. 1A, General Geology. In: Government Printing Office, The Hague, 732 pp. (especially v. 1A, p. 192–194, 197–200, 206–207).

van der Zwan, F.M., Chadwick, J.P., Troll, V.R., 2013. Textural history of recent basaltic-andesites and plutonic inclusions from Merapi volcano. Contrib. Mineral. Petrol. 166, 43–63. https://doi.org/10.1007/s00410-013-0864-7.

van Zalinge, M.E., Cashman, K.V., Sparks, R.S.J., 2018. Causes of fragmented crystals in ignimbrites: a case study of the Cardones ignimbrite, Northern Chile. Bull. Volcanol. 80, 22. https://doi.org/10.1007/s00445-018-1196-2.

Viccaro, M., Giacomoni, P.P., Ferlito, C., Cristofolini, R., 2010. Dynamics of magma supply at Mt. Etna volcano (Southern Italy) as revealed by textural and compositional features of plagioclase phenocrysts. J. Volcanol. Geotherm. Res. 116, 77–91. https://doi.org/10.1016/j.lithos.2009.12.012.

Walker, G.P., Self, S., Wilson, L., 1984. Tarawera 1886, New Zealand – A Basaltic Plinian Fissure Eruption. J. Volcanol. Geotherm. Res. 21, 61–78. https://doi.org/10.1016/0377-0273(84)90016-7.

Wen, S., Nekvasil, H., 1994. SOLVCALC: an interactive graphics program package for calculating the ternary feldspar solvus and for two-feldspar geothermometry. Comput. Geosci. 20, 1025–1040. https://doi.org/10.1016/0098-3004(94)90039-6.

Widiyantoro, S., Ramdhan, M., Métaxian, J.P., Cummins, P.R., Martel, C., Erdmann, S., Nugraha, A.D., Budi-Santoso, A., Laurin, A., Fahmi, A.A., 2018. Seismic imaging and petrology explain highly explosive eruptions of Merapi Volcano, Indonesia. Sci. Rep. 8, 13656. https://doi.org/10.1038/s41598-018-31293-w.

Woods, A.W., 1995. A model of vulcanian explosions. Nucl. Eng. Des. 155 (1–2), 345–357. https://doi.org/10.1016/0029-5493(94)00881-X.

Yokoyama, I., 2005. Growth rates of lava domes with respect to viscosity of magmas. Ann. Geophys. 48 (6), 957–971.

Zhang, Y., Behrens, H., 2000. H_2O diffusion in rhyolitic melts and glasses. Chem. Geol. 169, 243–262. https://doi.org/10.1016/S0009-2541(99)00231-4.

Journal of Volcanology and Geothermal Research

Supports *open access*

Submit your article

Menu

Search in this journal

Volume 443

November 2023

Download full issue

Previous vol/issue

Next vol/issue

Receive an update when the latest issues in this journal are published

Sign in to set up alerts

Full text access

Editorial Board

Article 107952

View PDF

FEEDBACK

Article 107914

View PDF Article preview

Research article ○ Abstract only

Provenance and depositional environment of Middle Miocene silicic volcaniclastic deposits from Mt. Medvednica (North Croatian Basin, Carpathian-Pannonian Region)

Nina Trinajstić, Mihovil Brlek, Sean P. Gaynor, Julie Schindlbeck-Belo, ... Réka Lukács
Article 107917

Article preview

Research article ○ Abstract only

Remote volcano monitoring using crowd-sourced imagery and Structure-from-Motion photogrammetry: A case study of Oldoinyo Lengai's active pit crater since the 2007–08 paroxysm

Pierre-Yves Tournigand, Benoît Smets, Kate Laxton, Antoine Dille, ... Matthieu Kervyn
Article 107918

Article preview

Research article ○ Abstract only

Dynamics of the Young Merapi (<2.2 ka – 1,788 CE) pumice fall deposits: Insights from textural and geochemical studies

Indranova Suhendro, Gabriela Nogo Retnaningtyas Bunga Naen, Andriansyah Gurusinga, Sistien Adhaena Sari, ... Dini Nuari Ardian
Article 107919

Article preview

Journal of Volcanology and Geothermal Research

Submit your article

View PDF Article preview

Research article ○ Abstract only

Diffuse soil CO_2 emissions at rift volcanoes: Structural controls and total budget of the Olkaria Volcanic Complex (Kenya) case study

L. Cappelli, P.A. Wallace, A. Randazzo, P.M. Kamau, ... K. Fontijn
Article 107929

Article preview

Research article ○ Abstract only

Low-grade to extremely high-grade ignimbrites and associated deposits of the uppermost Schrikkloof Formation in the Paleoproterozoic Rooiberg Group, Bushveld large igneous province, South Africa

Nils Lenhardt, Hannah S.R. Hughes, Lothar Viereck, Adam J. Bumby, ... Olutola O. Jolayemi
Article 107927

Article preview

Research article *Open access*

The noble gas signature of the 2021 Tajogaite eruption (La Palma, Canary Islands)

A. Sandoval-Velasquez, A.L. Rizzo, F. Casetta, T. Ntaflos, ... N.M. Pérez
Article 107928

View PDF Article preview

Research article ○ Abstract only

Research article *Open access*

The effects of hot and pressurized fluid flow across a brittle layer on the recent seismicity and deformation in the Campi Flegrei caldera (Italy)

Massimo Nespoli, Anna Tramelli, Maria Elina Belardinelli, Maurizio Bonafede
Article 107930

View PDF Article preview

Research article ○ Abstract only

Volcanic debris avalanche deposits and their significance in the architecture and evolution of the Miocene-Quaternary Călimani-Gurghiu-Harghita volcanic range (Eastern Transylvania, Romania)

Seghedi Ioan, Szakács Alexandru, Mirea Viorel, Pécskay Zoltán, Luffi Péter
Article 107932

Article preview

Research article ○ Abstract only

Magma and hydrothermal sources below the northern part of Paramushir Island (Kuril Arc) inferred from ambient noise tomography

Nadezhda Belovezhets, Yaroslav Berezhnev, Ivan Koulakov, Andrey Jakovlev, ... Ilyas Abkadyrov
Article 107931

Article preview

Research article ○ Abstract only

Journal of Volcanology and Geothermal Research

Submit your article

Research article ○ Abstract only

Seismic structure beneath the Avacha and Koryaksky volcanoes in Kamchatka based on the data of permanent and temporary networks

Elena Kitsura, Ivan Koulakov, Társilo Girona, Andrey Jakovlev, ... Mamdouh S. Alajmi
Article 107937

Article preview

Research article ○ Abstract only

Chemical and thermal changes in hot spring waters and fumarolic gases related to volcanic unrest at Meakandake volcano, Japan: Results of long-term geochemical monitoring from 1986 to 2022

Ryo Takahashi, Tagiru Ogino, Kazuto Ohmori, Yasuji Murayama
Article 107934

Article preview

Research article ○ Abstract only

Preliminary magnetotelluric investigation of crustal magma plumbing system beneath the Wulanhada volcanic field, northern China: Implications for the Magma reservoir and pathway

Zeyi Dong, Qibin Xiao, Yan Deng, Bing Han, ... Jijun Wang
Article 107938

Article preview

Journal of Volcanology and Geothermal Research

Submit your article

ELSEVIER

RELX™

ScienceDirect®

Journal of Volcanology and Geothermal Research

Supports *open access*

6.2	2.9
CiteScore	Impact Factor

Submit your article

Guide for authors

Menu

Search in this journal

- **Aims and scope**
- Editorial board
- Announcements
- Special Issue Proposals
- Policies and Guidelines

Aims and scope

An international research journal with focus on volcanic and geothermal processes and their impact on the environment and society.

Submission of papers covering the following aspects of volcanology and geothermal research are encouraged:

FEEDBACK

(1) Geophysical aspects of volcanic systems: physical properties of volcanic rocks, silicate melts, and magmas; heat flow studies; volcano seismology, geodesy and remote sensing.

(2) Volcano hazard and risk research: hazard zonation methodology, development of forecasting tools; assessment techniques for vulnerability and impact.

(3) Computational modeling and experimental simulation of magmatic and hydrothermal processes: eruption dynamics; magma transport and storage; plume dynamics and ash dispersal; lava flow dynamics; hydrothermal fluid flow; thermodynamics of aqueous fluids and melts.

(4) Geological and geochemical measurements of active volcanic systems and volcanic processes: volcano stratigraphy, eruptive history; evolution of volcanic landforms; eruption style and progress; dispersal patterns of lava and ash; analysis of real-time eruption observations, volatile compositions and degassing; textural analysis of volcanic rocks.

(5) Hydrology, geochemistry and measurement of magmatic, volcanic and hydrothermal fluids (the latter only if these propose novel aspects and processes of volcano-hosted hydrothermal systems); monitoring and modelling of volcanic gas emissions (including direct, in-situ, and remote measurements) and diffuse degassing (soils and springs/aquifers); crater lakes; hydrothermal mineralization.

The journal does not accept geothermal or other research papers that are not related to volcanism.

ELSEVIER

RELX™

Journal of Volcanology and Geothermal Research

Supports *open access*

Submit your article

Menu

Search in this journal

- Aims and scope
- **Editorial board**
- Announcements
- Special Issue Proposals
- Policies and Guidelines

Gender diversity of editors

71% man

FEEDBACK

Journal of Volcanology and Geothermal Research

Submit your article

Editorial board by country/region

39 editors and editorial board members in 15 countries/regions

1 United States of America (8)
2 United Kingdom (6)
3 Italy (5)

› See more editors by country/region

Editorial board

Co Editors-in-Chief

Associate Editor

Editorial Board Members

Journal of Volcanology and Geothermal Research

Submit your article

Journal of Volcanology and Geothermal Research

Submit your article

Journal of Volcanology and Geothermal Research

Submit your article